Energy & Environmental Science

ROYAL SOCIETY OF CHEMISTRY

PAPER

View Article Online
View Journal

Cite this: DOI: 10.1039/d3ee01606d

Analysis of bipolar membranes for electrochemical CO_2 capture from air and oceanwater†

Justin C. Bui, [ab] Éowyn Lucas, [cd] Eric W. Lees, [b] Andrew K. Liu, [ab] Harry A. Atwater, [cd] Chengxiang Xiang, [c] Alexis T. Bell [ab] and Adam Z. Weber *[b]

Received 18th May 2023,
Accepted 11th September 2023

DOI: 10.1039/d3ee01606d

rsc.li/ees

Carbon dioxide (CO_2) must be removed from the atmosphere to mitigate the negative effects of climate change. However, the most scalable methods for removing CO_2 from the air require heat from fossil-fuel combustion to produce pure CO_2 and continuously regenerate the sorbent. Bipolar-membrane electrodialysis (BPM-ED) is a promising technology that uses renewable electricity to dissociate water into acid and base to regenerate bicarbonate-based CO_2 capture solutions, such as those used in chemical loops of direct-air-capture (DAC) processes, and in direct-ocean capture (DOC) to promote atmospheric CO_2 drawdown *via* decarbonization of the shallow ocean. In this study, we develop an experimentally validated 1D model for the electrochemical regeneration of CO_2 from bicarbonate-based carbon capture solutions and seawater using BPM-ED. For DAC, our experimental and computational results demonstrate that pH swings induced by BPM water dissociation drive the formation of CO_2 at the cation-exchange layer|catholyte interface with energy-intensities of less than 150 kJ mol^{-1}. However, high rates of bubble formation increase energy intensity at current densities >100 mA cm^{-2}. Correspondingly, accelerating water dissociation catalysis and enacting bubble removal could enable CO_2 recovery at energy intensities <100 kJ mol^{-1} and current densities >100 mA cm^{-2}. For DOC, mass transport limitations associated with low carbon concentrations in oceanwater suggest that DOC is best suited for clean production of acid and base usable in downstream processes. These results provide design principles for industrial-scale CO_2 recovery using BPM-ED.

Broader context

Bipolar-membrane electrodialysis (BPM-ED) carbon capture uses renewable electricity to drive the capture and release of carbon dioxide (CO_2), making it a potentially valuable tool in the fight against climate change. This process employs BPMs to generate pH-swings for CO_2 capture and has been demonstrated at the lab scale at current densities exceeding 100 mA cm^{-2}. However, the energy required to drive BPM-ED (>300 kJ mol^{-1}) is prohibitive for industrial deployment. This study optimizes BPM-ED using a continuum modeling approach validated by experiment, which quantifies the energy intensity of BPM-ED and resolves the transport and dynamic equilibrium of reactive carbon species in BPMs. Applied-voltage-breakdown analysis identifies the dominant energy losses and elucidates BPM properties that improve the efficiency of BPM-ED. The model reveals that mitigation of generated CO_2 bubbles and acceleration of water-dissociation catalysis could reduce the energy intensity to <80 kJ mol^{-1} at 100 mA cm^{-2} in $KHCO_3$ electrolytes, demonstrating potential for achieving high rates with substantially reduced energy penalties. This study provides insights into the physics of BPMs immersed in reactive carbon solutions and contributes towards the development of BPMs for electrochemical CO_2 reduction, cement production, and other emerging electrochemically decarbonized applications.

[a] *Department of Chemical and Biomolecular Engineering, University of California Berkeley, Berkeley, CA 94720, USA*
[b] *Liquid Sunlight Alliance, Lawrence Berkeley National Laboratory, Berkeley, CA 94720, USA. E-mail: azweber@lbl.gov; Tel: +1-(510)-486-6308*
[c] *Liquid Sunlight Alliance, California Institute of Technology, Pasadena, CA 91125, USA*
[d] *Department of Applied Physics, California Institute of Technology, Pasadena, CA 91125, USA*

† Electronic supplementary information (ESI) available. See DOI: https://doi.org/10.1039/d3ee01606d

1. Introduction

Carbon-dioxide (CO_2) emissions account for 76% of total greenhouse-gas emissions and are currently 50% higher than pre-industrial levels. As a result, temperatures are expected to rise at least 2 °C unless CO_2 is captured and removed from the atmosphere.[1–3] Traditional direct-air-capture technologies (DAC),[4] use alkaline aqueous sorbents (*e.g.*, $KOH_{(aq)}$) to capture

ambient CO_2 as mixtures of (bi)carbonates, which are thermally-decomposed into a pure CO_2 gas stream for permanent removal (Fig. 1a). Unfortunately, this technology is energy intensive and expensive, largely because of the significant thermal energy penalty (>150 kJ mol^{-1}) required to regenerate the sorbent after it has captured CO_2 (Fig. 1a, step 4).[5] This thermal energy is often provided by burning natural gas, which results in CO_2 emissions that reduce the net amount of CO_2 removed from the atmosphere by DAC.

Electrochemically-mediated carbon capture (EMCC) can address the challenges associated with thermal sorbent regeneration by using low-cost renewable electricity to trigger the capture and release of CO_2 from the sorbent.[2,6–17] The low-temperature nature of EMCC also circumvents the thermal efficiency limits associated with desorbing CO_2 at high-temperature in fired reboilers and calciners.[18] Many chemistries have been explored for EMCC, such as nucleophilic sorbents that can absorb or desorb CO_2 when oxidized or reduced at an electrode surface[2,14,19,20] and amine-based sorbents that capture CO_2 homogeneously and release that CO_2 upon the reaction with cupric (Cu^{2+}) ions generated *via* electrochemical redox.[21,22] However, these specific EMCC

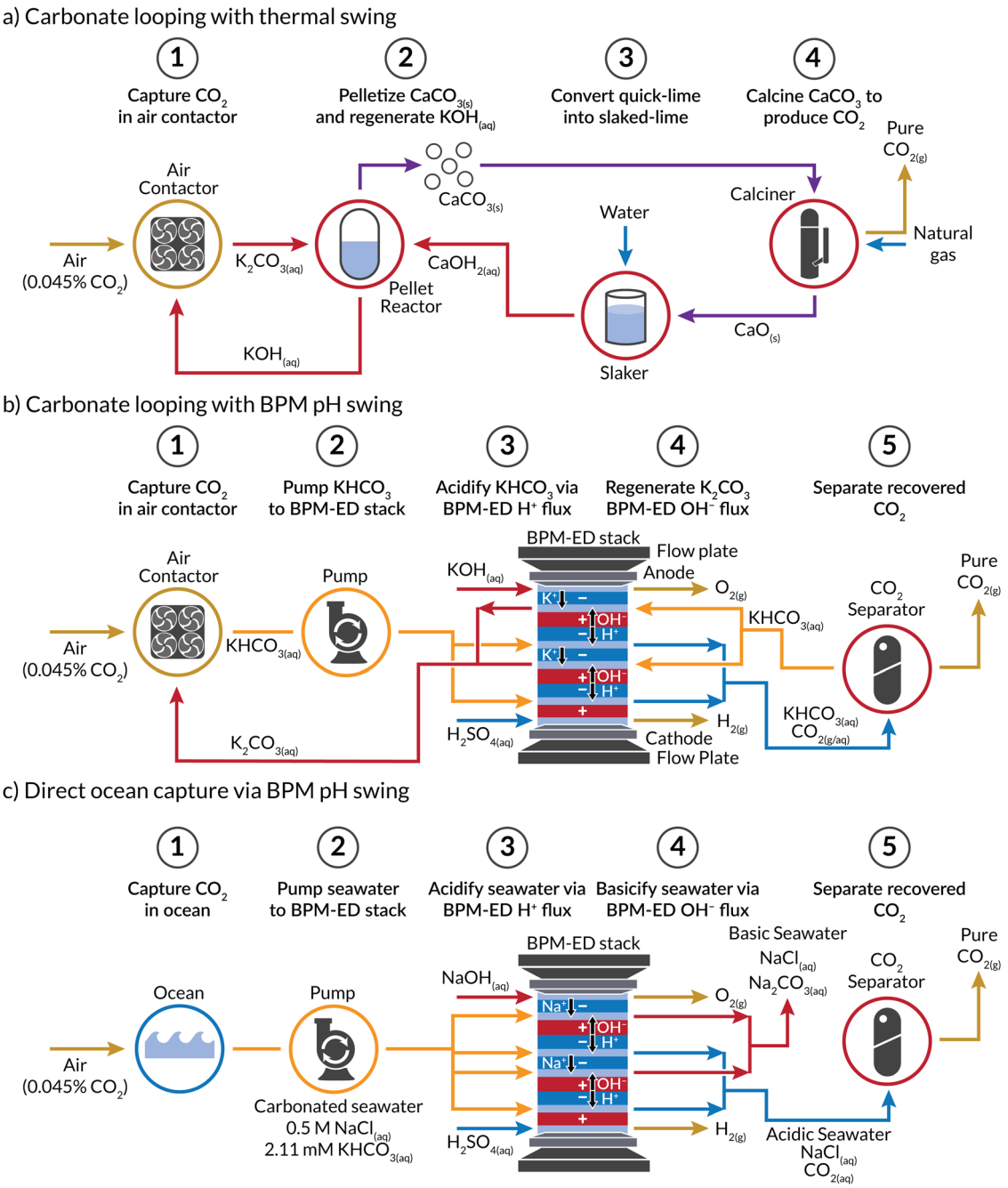

Fig. 1 Process flow diagrams of various carbon capture processes. (a) Carbonate looping with thermal swing desorption. (b) Carbonate looping with electrochemical pH swing desorption *via* BPM-ED. (c) Direct ocean capture with electrochemical pH swing desorption *via* BPM-ED.

technologies have not been demonstrated at current densities beyond 5 mA cm^{-2}, necessitating large, costly reactors or long residence times.[23,24]

Bipolar-membrane electrodialysis (BPM-ED) is a promising EMCC technology that uses water dissociation to mediate CO_2 capture and sorbent regeneration at relevant current densities (*i.e.*, >100 mA cm^{-2}; Fig. 1b).[16,17,25] At the heart of this technology is a BPM, which consists of anion- and cation-exchange layers (AEL and CEL) that are laminated together often with a catalyst layer (CL) at the interface. Under a reverse bias, the strong electric field formed at the interface of the oppositely-charged AEL and CEL layers drives water dissociation into acid (H^+) and base (OH^-) (eqn (1)).[26,27] The acid produced in the CEL is used to shift the equilibrium distribution among bicarbonate, carbonate, and CO_2 (eqn (2)–(5)) towards CO_2,[26,28] and the base produced in the AEL is used to regenerate the alkalinity of the carbonate sorbent. A key advantage of BPM-ED is the use of water as the reactant, which enables higher current densities than other EMCC technologies because of the high concentration of water (55 M) in aqueous CO_2 capture solutions. Notwithstanding, the energy intensity of BPM-ED typically exceeds 300 kJ mol^{-1} because of the water dissociation overpotential and ohmic resistance of the BPM. Further optimization is therefore required for BPM-ED to become more efficient than thermal CO_2 sorbent regeneration.[24]

An alternative is to employ BPM-ED to extract CO_2 from the inherent (bi)carbonate content of seawater (Fig. 1c), *i.e.*, direct ocean capture (DOC).[7,16,17,25,29,30] By using seawater as the sorbent, instead of a $KHCO_3$ solution, the natural process of CO_2 absorption and conversion into bicarbonates is leveraged and obviates the need for a Capex-intensive air contactor.[4] In the DOC configuration, the OH^- transported from the AEL can be reacted with dissolved bicarbonates in the seawater to form a mineralized carbonate stream that can be precipitated and sequestered, or fed back into the ocean to help reverse the effects of ocean acidification.[31] CO_2 that is formed by BPM-ED can be collected outside the device for conversion or storage elsewhere,[7] or transported directly to a CO_2 reduction catalyst within the same device for direct conversion.[28,32]

The challenge with BPM-ED is that the energy intensities reported in the literature (300 to 1000 kJ mol^{-1} CO_2) are significantly higher than the minimum thermodynamic energy required to separate CO_2 from air (20 kJ mol^{-1}).[8] Unfortunately, while the mechanism of *in situ* CO_2 capture and sorbent regeneration *via* BPM-ED has been well established experimentally,[32–34] very few theoretical studies have simulated BPMs immersed in carbon-containing solutions to resolve the dominant energy losses. Sabatino *et al.* developed process-level simulations to show the critical role BPM performance has on the energy intensity and overall technoeconomic feasibility of BPM-ED EMCC.[35,36] However, the simulations treated the BPM as a black-box, with no information provided regarding ionic transport, water dissociation kinetics, or the material properties of the BPM that would be required to achieve the necessary performance enhancements. In both DAC and DOC, facilitating an understanding of both the transport of reactive carbon species and the associated kinetics of their buffer reactions will be critical to advancing the nascent technologies.

Continuum models by Lees *et al.* and Kas *et al.* have helped to resolve the mechanism of *in situ* CO_2 generation in BPM-based electrolyzers that convert (bi)carbonate capture solutions to carbon monoxide,[37,38] or methane.[28] However, these models only considered the CEL of the BPM, ignoring the AEL and the water dissociation CL where protons and hydroxide are generated. This simplification renders the models incapable of predicting the primary factors influencing the energy intensity of BPM-ED: carbon crossover, water dissociation overpotential, and ohmic loss.[39,40] There is also little precedent for modeling the transport of dilute carbon species in seawater feedstocks used for DOC.[7,41] Models that relate the chemistry and material properties of BPMs to the energy intensity of BPM-ED are therefore warranted.[42]

In this work, we demonstrate a comprehensive model of BPM-ED based on our prior work modeling multi-component transport in BPMs,[27] now with the homogeneous reaction kinetics of reactive carbon species (eqn (2)–(5)). The model is validated by comparison with experimental data for various carbon-containing solutions and is used to elucidate the nature of *in situ* CO_2 generation and sorbent regeneration in BPMs employed for EMCC. Additionally, concentration profiles and fluxes of all carbon species, protons, and hydroxide anions are resolved such that performance tradeoffs between CO_2 generation and carbon crossover can be explored. Lastly, sensitivity analysis provides improved understanding of ideal BPM and system properties to enhance CO_2 capture efficiency, setting the stage for BPMs optimized for carbon capture processes.

2. Methods

2.1. Theory and computational methods

The BPM model employed here (described in detail in Section S1 of the ESI†) was designed to mimic the 4-probe experiments performed for direct BPM analysis (described in detail in Section 2.2), modeling the relevant domain as a 1-dimensional (1D) continuum consisting of an 80 μm CEL, and an 80 μm AEL sandwiching a 3.5 nm water dissociation CL, with a 25 μm diffusion boundary layer (Section S1.6, ESI†) on either side of the BPM assembly (Fig. 2). Modeling the domain as such enables the capturing of all relevant concentration profiles and species fluxes. Importantly, the model also explicitly considers the generation and consumption of species *via* the homogeneous buffer reactions shown below. The effects of forced convection on the transport of CO_2 and ions are considered implicitly *via* the thickness of the diffusion boundary-layer, but convective effects are not considered explicitly within the modeled domain, because the model is 1-D in the through-plane direction perpendicular to the direction of flow. It is important to note that the experiments were carried out at ambient temperature (298 K) and, accordingly, all simulations were carried out at this temperature. Hence, the effects of temperature were not considered. We note that the operating temperature will affect CO_2

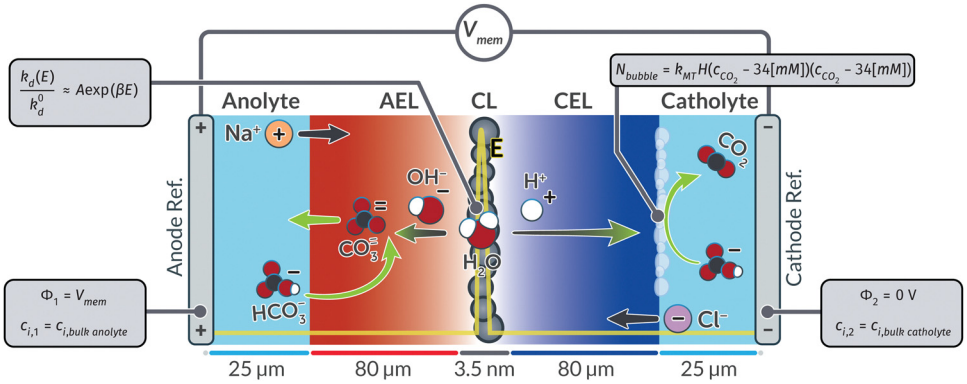

Fig. 2 Schematic of simulated domain for BPM performing BPM-ED EMCC. H_2O at the interface of the AEL and CEL (in the CL) is reacted by electric-field-enhanced water dissociation to form H^+ and OH^-. The H^+ reacts with HCO_3^- in the catholyte to form CO_2. Once the *in situ* generated CO_2 has exceeded its solubility limit in the catholyte, it exits the aqueous phase in the form of bubbles. OH^- from water dissociation reacts with HCO_3^- absorbed in the AEL to form CO_3^{2-} that transports back into the anolyte. Spectator co-ions from the anolyte or catholyte can cross through the membrane to reduce the developed pH gradient.

solubility, water dissociation kinetics, and BPM stability. However, these effects were not explored and are beyond the scope of the present work.

$$H_2O \overset{k_1,k_{-1}}{\longleftrightarrow} H^+ + OH^- \quad K_1 = 1 \times 10^{-14} \tag{1}$$

$$CO_{2(aq)} + H_2O_{(l)} \overset{k_2,k_{-2}}{\longleftrightarrow} H_{(aq)}{}^+ + HCO_{3(aq)}{}^- \quad K_2 = 4.27 \times 10^{-7} \tag{2}$$

$$HCO_3^- \overset{k_3,k_{-3}}{\longleftrightarrow} H^+ + CO_3^{2-} \quad K_3 = 4.58 \times 10^{-11} \tag{3}$$

$$CO_{2(aq)} + OH^- \overset{k_4,k_{-4}}{\longleftrightarrow} HCO_3^- \quad K_4 = 4.27 \times 10^{7} \tag{4}$$

$$HCO_3^- + OH^- \overset{k_5,k_{-5}}{\longleftrightarrow} H_2O + CO_3^{2-} \quad K_5 = 4.58 \times 10^{3} \tag{5}$$

The simulated membrane potential across the 1D domain is equivalent to the measured membrane potential across the two reference electrodes in the 4-probe experiment. The choice of a 4-probe measurement (and simulation) is critical because it enables the decoupling of the potential losses that occur at the anode and cathode from those that result from and drive transport and kinetics in the BPM.[43] For the purposes of the simulations and energy intensity calculations, we defined the energy intensity of the BPM-ED processes as the membrane potential in the 4-probe experimental cell since the energetics of the terminal electrodes are not directly correlated with the rate of CO_2 efflux or sorbent regeneration in the BPM. Moreover, the terminal electrodes are often used to perform reactions that produce value-added streams in EMCC processes.[28,34] Terminal electrodes were considered in our BPM-ED stack analysis (Section S24, ESI†) to compare the associated energy penalty to the overall cell voltage as the number of BPMs in the stack is increased.[30] We note that this energy intensity does not include the energy due to electrolyte pumping. However, this energy will be relatively small ($\sim$4.4 kJ mol^{-1} in thermal DAC processes) in comparison to the energy required to perform BPM-ED (>100 kJ mol^{-1}).[44] It is also important to note that CO_2 regeneration from acidified bicarbonate solutions occurs spontaneously,[44] so no additional energy input is required beyond the process of making acid and base in the BPM.

2.1.1. Thermodynamics of BPM-ED EMCC. To describe the thermodynamics of all species within the BPM, the following electrochemical potential expression is used[45,46]

$$\mu_i = \mu_i^0 + RT\ln(a_i) + z_iF\Phi, \tag{6}$$

where ϕ is the electrostatic potential within the electrolyte and membrane phases and R, T and F are the ideal gas constant, the temperature, and Faraday's constant, respectively. In the above expression, the first term is the reference chemical potential of species i, the second term accounts for changes in activity of i, the third term accounts for electrostatic potential and only applies for charged ionic species (*i.e.*, all species except CO_2). The activity (a_i) of a given species is defined by

$$a_i = \frac{f_i c_i c^0_{H_2O}}{c_{ref} c_{H_2O}}, \tag{7}$$

where c_{ref} is a reference concentration (1 M), and the ratio $\frac{c_{H_2O}}{c^0_{H_2O} = 55.56[M]} = \varepsilon_w$ is the water volume fraction and accounts for change in volumetric reference between the liquid electrolyte and liquid-filled channels of the BPM; in other words, equilibrium is calculated and upheld within the interstitial volume of the BPM. Note that ion specific partitioning was not considered in the model as the relevant parameters are currently unavailable. The activity coefficient (f_i) for charged species that participate in homogeneous buffer reactions (HCO_3^-, CO_3^{2-}, H^+, and OH^-) is a function of the electric field,

$$f_{i=OH^-,H^+CO_3^{2-}, \text{ or } HCO_3^-} = \sqrt{f(E)}^{-|z_i|}, \tag{8}$$

where $|z_i|$ is the absolute value of the charge on species i, E is the local electric field, and $f(E)$ is the dependence of the macroscopic equilibrium constant on electric field, defined by the second

Wien effect for net-charge-generating dissociation reactions (reactions (1)–(3) above).[26,47–50]

$$f(E) = \frac{\left(\sum_{m=0}^{\infty} \frac{1}{m!(m+1)!}(2\beta E)^m\right)\cosh(\tau\beta E)\cosh(\tau)^{\beta E}}{1 + \frac{1-\exp\left(-\frac{1}{\sigma}\right)}{2}\left(\sigma^2\beta E + (4.97\sigma)\frac{\sinh(0.0835\sigma\beta E)}{\cosh^2(0.0835\sigma\beta E)}\right)}. \quad (9)$$

where β, τ, and σ are lumped parameters discussed in more detail in Section S1.3 (ESI†). The dependence on E in eqn (9) is approximately exponential, as shown in previous work.[26] The above dependence of the activity coefficient on the electric field ensures that macroscopic equilibrium is upheld (*e.g.*, $\mu_{H^+} + \mu_{OH^-} = \mu_{H_2O}$ for water dissociation or $\mu_{H^+} + \mu_{CO_3^{2-}} = \mu_{HCO_3^-}$ for bicarbonate dissociation) (see Section S1.1, ESI† for consistency of macroscopic equilibrium), and results in the equilibrium constants of net-charge-generating reactions to be

$$K_{n=1,2,3}(E) = K_n(E=0)f(E) \quad (10)$$

where $K_{n=1,2,3}(E)$ is the equilibrium constant, which is a function of local electric field, and $K_n(E=0)$ is the value of the equilibrium constant for no applied electric field. For neutral species (*i.e.*, CO_2) and ions that do not participate in buffer reactions (*i.e.*, K^+), the activity coefficient is unaffected by the electric field. We note that ion-specific interactions likely impact ionic transport and concentrations in the BPM due to the high concentrations (>1 M) in the BPM.[51,52] However, these are likely second-order effects and mixed-interaction parameters are not available for the broad variety of ions in the polymer membranes studied herein.

2.1.2. Kinetics of BPM-ED EMCC. Homogeneous reactions consume carbon-containing species, OH^-, and H^+ throughout the electrolyte domain. The rate of consumption of species i in bulk reactions is given by the law of mass action:

$$R_{B,i} = \varepsilon_w \sum_n s_{i,n}\left(k_n \prod_{s_{i,n}<0} a_i^{-s_{i,n}} - k_{-n}\prod_{s_{i,n}>0} a_i^{s_{i,n}}\right) \quad (11)$$

Similar to how the macroscopic equilibrium is impacted by the electric field through the second Wien effect, the forward and reverse rate constants for net-charge-generating homogeneous reactions are affected by the electric field, with their electric-field-dependence taking the form of the numerator and denominator, respectively, of eqn (9).

$$\frac{k_n(E)}{k_n(E=0)} = \left(\sum_{m=0}^{\infty}\frac{1}{m!(m+1)!}(2\beta E)^m\right)\cosh(\tau\beta E)\cosh(\tau)^{\beta E} \quad (12)$$

$$\frac{k_{-n}(E)}{k_{-n}(E=0)} = 1 + \frac{1-\exp\left(-\frac{1}{\sigma}\right)}{2}\left(\sigma^2\beta E + (4.97\sigma)\frac{\sinh(0.0835\sigma\beta E)}{\cosh^2(0.0835\sigma\beta E)}\right) \quad (13)$$

To model the water dissociation catalyst, we treat the CL as a thin neutral region located between the AEL and CEL where the large field in between the two layers drives the dissociation of water by shifting the forward and reverse rate constants as per eqn (12) and (13). While more detailed models of water dissociation catalysis have been presented that explicitly consider catalyst surface effects,[26,53] we choose a more simple model for water dissociation for computational efficiency. Furthermore, the interaction of carbon species with catalyst surfaces are still not well understood; because this work is more focused on modeling the impact of reactive carbon species on polarization behavior and mesoscale transport, the exact details of the catalyst surface are not crucial to capture. More details on the choice of model for the CL can be found in Section S1.4 (ESI†).

2.1.3. Mass and charge conservation in BPM-ED EMCC. To solve for all concentrations and fluxes of relevant species (CO_2, OH^-, H^+, Cl^-, HCO_3^-, CO_3^{2-}, Na^+ and K^+), species conservation is used,

$$\nabla\cdot\boldsymbol{N}_i = R_{B,i}, \quad (14)$$

where $\boldsymbol{N}_i$ is the flux of species i, and $R_{B,i}$ is a source term defined as the generation of species i from homogeneous buffer reactions and water recombination/dissociation (described in detail in Section 2.1.2). The molar species flux is defined by the Nernst–Planck equation,

$$N_i = -\frac{D_i c_i}{RT}\frac{d\mu_i}{dx}, \quad (15)$$

where D_i, c_i, μ_i are the diffusivity, concentration, and electrochemical potential of species i, respectively. Fluxes due to the second Wien effect modification to the Poisson Nernst Planck equations are also directly calculated from the derivative of the Wien effect activity coefficient (eqn (8)).

The Poisson equation is solved to determine the electrostatic potential,

$$-\frac{d^2\Phi}{dx^2} = \frac{F}{\varepsilon}\left(c_M(x) + \sum_i z_i c_i\right), \quad (16)$$

ε is the dielectric permittivity of the medium, defined to be that of water (ε_{H_2O}) in the electrolyte domains. For the membrane domains, the dielectric permittivity is defined by eqn (S35) in the ESI.†

The diffusivities, permittivities, and transport properties are calculated as per previous work.[54] The double-layer thickness is simulated by solution of the Wien-effect modified PNP and results from an assumed neutralization thickness of 3.5 nm at the AEL|CEL interface.[27,55] Discussion of the double layer simulation at the AEL|CEL interface can be found in prior work.[27] Details on how the diffusivities and transport properties in the BPM are calculated can be found in Section S1.5 (ESI†).

2.1.4. Phase transfer due to bubbling and bubble coverage effects. To account for the bubbling out of CO_2 gas at the catholyte boundary-layer (cBL)|CEL interface, a phase transfer flux sink term is incorporated into the model that activates once the dissolved CO_2 concentration in the catholyte exceeds the saturation concentration (Fig. 2),

$$N_{\mathrm{PT,CO_2,CEL|cBL}} = k_{\mathrm{MT}} H(C_{\mathrm{CO_2,CEL|cBL}} - 34[\mathrm{mM}])(C_{\mathrm{CO_2,CEL|cBL}} - 34[\mathrm{mM}]) \quad (17)$$

where k_{MT} is a mass transfer coefficient set to 1×10^5 m s^{-1} to ensure that any dissolved CO_2 beyond saturation immediately bubbles out of the electrolyte. $H(x)$ is the Heaviside step function. $c_{\mathrm{CO_2,CEL|cBL}}$ is the concentration of dissolved CO_2 in the catholyte side of the CEL|cBL interface.

Because the model immediately removes bubble CO_2 from the domain and does not track the bubble phase explicitly, to determine the gas bubble flux out of the domain, the model is run with and without the flux term shown in eqn (17), and the flux of bubbles out of the domain ($j_{\mathrm{CO_2,bubble}}$) is determined as the difference in CO_2 efflux between the simulations with and without implementation of eqn (17) (Fig. S2, ESI†).

$$j_{\mathrm{bubble,CO_2}} = j_{\mathrm{CO_2,out,no\ phase\ transfer}} - j_{\mathrm{CO_2,out,with\ phase\ transfer}} \quad (18)$$

In accordance with prior work examining the effect of gas bubbling on electrochemical systems,[56] the CO_2 bubbles, which are quite substantial (see Video S1, ESI†), accumulate on the surface and reduce the electrochemically active surface area and consequently the current density that can be achieved. The bubble coverage ($\theta_{\mathrm{CO_2,bubble}}$) is related to the bubble efflux and can be calculated by[56]

$$\theta_{\mathrm{CO_2,bubble}} = 0.024\left(\frac{F \times j_{\mathrm{bubble,CO_2}}}{1[\mathrm{mA\ cm^{-2}}]}\right)^{0.55} \quad (19)$$

where the values of 0.024 and 0.55 in the above expression are fitted parameters that are consistent with prior implementations of the above model for bubble coverage.[56] The coverage term ($\theta_{\mathrm{CO_2,bubble}}$) calculated using this semi-empirical model represents a site-blocking factor equal to the fraction of the areal cross section impeded by bubbles and thus inaccessible for ionic transport. Thus, once ($\theta_{\mathrm{CO_2,bubble}}$) is calculated, the simulated current density is corrected to account for the loss in active area due to bubble coverage:

$$i_{\mathrm{BPM}} = i_{\mathrm{BPM,no\ bubble}}(1 - \theta_{\mathrm{CO_2,bubble}}) \quad (20)$$

where $i_{\mathrm{BPM,no\ bubble}}$ is the simulated BPM current density prior to post-processing with bubble coverage effects.

2.1.5. Boundary conditions. Boundary conditions are shown in the schematic in Fig. 2. At the end of anolyte boundary layer (leftmost boundary), Dirichlet boundary conditions set the concentrations of all modeled ionic species to their bulk electrolyte values,

$$c_i\big|_{x=-\frac{L_{\mathrm{CL}}}{2}-L_{\mathrm{AEL}}-L_{\mathrm{cBL}}} = c_{i,\mathrm{anolyte}}^{\mathrm{bulk}} \quad (21)$$

where the origin ($x = 0$) is defined at the center of the CL, L_{CL} is the CL thickness, L_{AEL} is the AEL thickness, and L_{aBL} is the anolyte boundary-layer (aBL) thickness. The thickness of both the catholyte and anolyte boundary layers are assumed to be equal to 25 μm and are estimated by assuming approximately Fickian behavior of the CO_2 at the onset of bubbling (Section S1.6, ESI†).

The electrostatic potential is set to the measured membrane potential with another Dirichlet boundary condition,

$$\Phi\big|_{x=-\frac{L_{\mathrm{CL}}}{2}-L_{\mathrm{AEL}}-L_{\mathrm{aBL}}} = V_{\mathrm{mem}} \quad (22)$$

At the end of the cBL (rightmost boundary), Dirichlet boundary conditions are again employed to set species concentrations to their bulk values (as defined by their equilibrium concentrations for the given (bi)carbonate salt concentration):

$$c_i\big|_{x=\frac{L_{\mathrm{CL}}}{2}+L_{\mathrm{CEL}}+L_{\mathrm{cBL}}} = c_{i,\mathrm{catholyte}}^{\mathrm{bulk}} \quad (23)$$

L_{CEL} is the CEL thickness, and L_{cBL} is the cBL thickness. Lastly, the electrostatic potential is set to a reference of 0 V at the catholyte boundary,

$$\Phi\big|_{x=\frac{L_{\mathrm{CL}}}{2}+L_{\mathrm{CEL}}+L_{\mathrm{cBL}}} = 0\ \mathrm{V} \quad (24)$$

2.1.6. Computational methods. The governing equations representing this model were solved using two coupled General Partial Differential Equation (g) Modules in COMSOL Multiphysics 5.6. The modeling domain was discretized with a nonuniform mesh with heavy refinement near all interfaces (membrane–membrane, membrane–electrolyte, and membrane–CL) as well as within the CEL and catholyte where *in situ* CO_2 generation occurs. The resulting mesh comprised 6000–18 000 elements depending on the applied current density. A mesh independence study was performed, and the results were found to be independent of meshing for those meshes. Critically, to achieve initial convergence, the Donnan equilibria were solved analytically to obtain species concentrations in each of the membrane layers at 0 applied membrane potential and fed to the simulation as initial conditions using hyperbolic tangent analytic functions. The simulations in the present study were solved using the Multifrontal Massively Parallel sparse direct Solver (MUMPS) using Newton's Method with a tolerance of 0.001 and a recovery damping factor of 0.75. For current densities where bubbling occurs, due to numerical instability, the tolerance was increased to 0.008 and the recovery damping factor reduced to 0.35.

2.2. Experimental methods

2.2.1. Chemicals. All chemicals were used as purchased. Sodium hydroxide (NaOH, Macron Chemicals), sodium chloride (NaCl, VWR Chemicals), sodium bicarbonate ($NaHCO_3$, ≥99.5%, Sigma-Aldrich), potassium bicarbonate ($KHCO_3$, 99.7–100.5%, J. T. Baker), and potassium carbonate (K_2CO_3, 99.997%, Thermo Scientific). Simulated seawater in this work consists of 0.5 M NaCl with 0.00211 M $NaHCO_3$.

2.2.2. Electrodialysis cell. Experimental current density–voltage measurements were obtained using a home-made five-chamber electrodialysis cell with Luggin capillaries. The cell was constructed, as depicted in Fig. S1 (ESI†), using a Ni foil (VWR) anode and cathode, Nafion N324 CEMs (FuelCellStore), Fumasep FAB-PK-130 AEM (Fuelcellstore), and Fumasep FBM-PK BPM (FuelCellStore). The active area of the BPM in this specific cell was one cm^2. Copper tape was used as leads for the Ni electrodes and Ag/AgCl (CH instruments, CHI111P) reference electrodes were placed in custom made glass Luggin capillaries on either side of the BPM.

2.2.3. Electrochemical measurements. Once the electrodialysis cell was assembled, a peristaltic pump (Ismatec ISM4408) was used to flow 1 M NaOH (10 mL min^{-1}) through the outer chambers, 3 M NaCl (10 mL min^{-1}) through the dilute chamber (chamber between CEM and AEM), and the relevant bicarbonate, carbonate, or simulated seawater solution (0.2 mL min^{-1}) through the chambers on either side of the BPM. These flowrates remained constant through all measurements. Once all chambers were filled, leads from a SP-300 BioLogic potentiostat were connected to the cathode, anode, and reference electrodes in a four-probe measurement configuration. Current density–voltage measurements were then obtained by applying a chosen current across the cathode and anode and measuring the voltage between the two Ag/AgCl reference electrodes. Oxygen evolution was performed at the anode and hydrogen evolution was performed at the cathode. These reactions were isolated from the BPM with the two monopolar membranes positioned on either side. Measurements were started at 0.1 mA cm^{-2} and increased stepwise through each current density to 100 mA cm^{-2} (EC-lab® software). Each current step was held constant for 20 minutes to obtain a steady-state voltage. The final voltage collected at each current step was reported in the current density–voltage plots, except for some of the higher current density steps. During the 1 M $KHCO_3$ and 0.5 M $KHCO_3$ experiments, CO_2 bubbles formed at the surface of the electrode at higher current densities ($\geq$20 mA cm^{-2}) causing a significant amount of noise in the data. For these measurements, the voltage reported was taken as the average over the current step.

3. Results and discussion

3.1. Agreement with experiment and breakdown of partial current density

To understand the transport and reaction kinetics of reactive carbon species in BPMs, experimental polarization curves were taken in a 4-probe experimental cell for a BPM immersed in three electrolytes relevant to EMCC and DOC applications: 1 M $KHCO_3$, 0.5 M $KHCO_3$, and simulated seawater (0.00211 M $NaHCO_3$ + 0.5 M NaCl). Simulations of the BPM under polarization in these varying electrolytes were run and the simulated polarization curves were compared to the experimentally measured polarization curves (Fig. 3a, markers). In these experiments and simulations, the electrochemical bias reported is the measured electrostatic potential drop across the BPM and the associated diffusion boundary layers, which contains the voltage required to drive ionic transport through each layer, the voltage required to generate the pH gradient across the AEL|-CEL interface, and the kinetic overpotential for the water dissociation reactions, as well as the voltage losses associated with CO_2 bubble formation. Strong agreement between theory and experiments is observed in all three carbon-containing electrolytes for a single set of fitting parameters (Table S5, ESI†). Remarkably, the simulation can even capture the incredibly non-intuitive polarization behavior occurring at current densities <20 mA cm^{-2} (Fig. S3, ESI†). For these current densities, there is an initial onset in current density at ~0.4 V of applied membrane potential for both the 0.5 M $KHCO_3$ and 1 M $KHCO_3$ BPMs. The current density of these BPMs increases approximately linearly until ~0.7 V when the

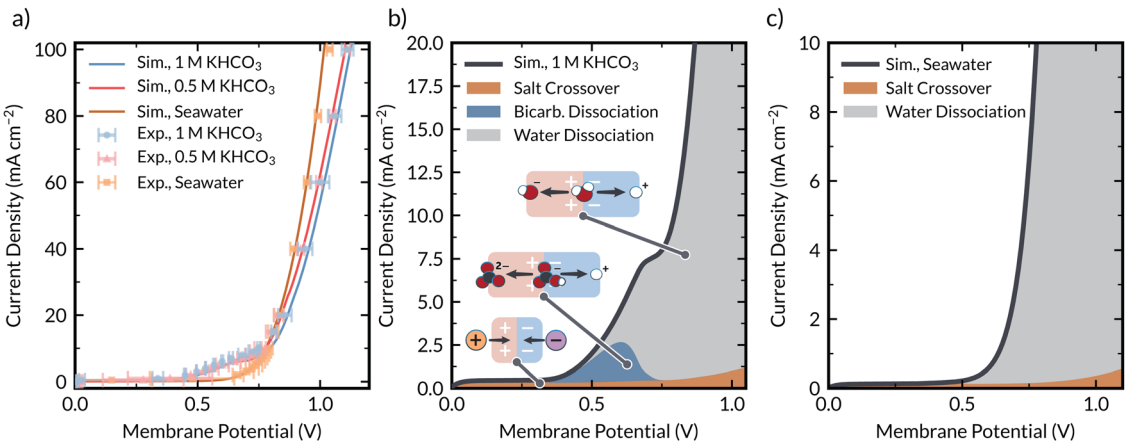

Fig. 3 (a) Experimental (markers with error bars) and simulated (solid lines) polarization curves for BPMs immersed in various solutions of aqueous bicarbonate. (b) and (c) Breakdown of partial current density in the CL due to contributions of salt crossover (orange), bicarbonate dissociation (blue), and water dissociation (gray) for a BPM immersed in (b) 1 M $KHCO_3$ and (c) simulated seawater. The *y*-scale for panels (b) and (c) are zoomed in to highlight the unique behavior of the carbon-containing BPMs at low current densities.

current density takes off exponentially. Conversely, for the seawater BPM, the current density does not have an initial takeoff at 0.4 V, so between 0.4 and 0.8 V the seawater BPM drives less current density than the $KHCO_3$ BPMs. However, past the second onset at ~0.7 V, the current generated in the seawater BPM exceeds that of the $KHCO_3$ BPMs. Notably, the initial linear takeoff of the $KHCO_3$ BPMs at 0.4 V of membrane potential, along with the intriguing intersection and crossover between the seawater and (bi)carbonate polarization curves at ~0.75 V, represent heretofore unexplained phenomena that the model is capable of replicating with high accuracy.

To uncover the origin behind these phenomena and deconvolute the individual contributions to the polarization curves of BPMs in reactive carbon solutions, the rates of the individual contributions to current density were calculated within the CL of the BPM. Within the CL, the current density must either be due to the crossover of unreactive co-ions (K^+, Na^+, or Cl^-), or to the presence of electric-field-enhanced, net-charge-generating dissociation reactions. These contributions to the overall polarization curve are determined and shown in Fig. 3b and c for BPMs operating in 1 M $KHCO_3$ and simulated seawater, respectively. As expected, the current density for the simulated seawater case is primarily driven by salt crossover at low potentials and water dissociation at high potentials, as shown in previous literature.[27,45] The 1 M $KHCO_3$ case, however, is more intriguing. While previous studies have suggested that the low applied potential current onset for BPMs in weak buffer electrolytes is entirely driven by titration currents resulting from dissociation of the weak acid buffer (*i.e.*, the HCO_3^- anion in this case) in the CL,[27,50,57] the model suggests that current density in the initial linear feature is still primarily dominated by field-enhanced water dissociation. Field-enhanced dissociation of the buffering anion accounts for up to 50% of the observed current density. Therefore, the model suggests that the use of 1 M $KHCO_3$ buffer electrolytes forces an early onset of the electric-field-enhanced water-dissociation reaction.

The simulations demonstrate that the accelerated current onset for $KHCO_3$-exchanged BPMs is largely due to a reduction in the rate of interfacial recombination due to reaction of water-dissociation-generated OH^- with HCO_3^- to form CO_3^{2-} *via* what is essentially an indirect HCO_3^- dissociation pathway (water dissociation followed by bicarbonate to carbonate interconversion), and that the eventual increase of the seawater current density beyond the $KHCO_3$ current densities is due to the seawater BPM possessing a larger electric field at a given membrane potential (see Section S6, ESI† for more detail regarding the reasoning for the observed curvature of the BPM polarization curves in these carbon containing electrolytes).

3.2. Simulated concentration profiles of ionic species and CO_2

The validated model was employed to resolve local concentrations and microenvironments within BPMs exchanged with the

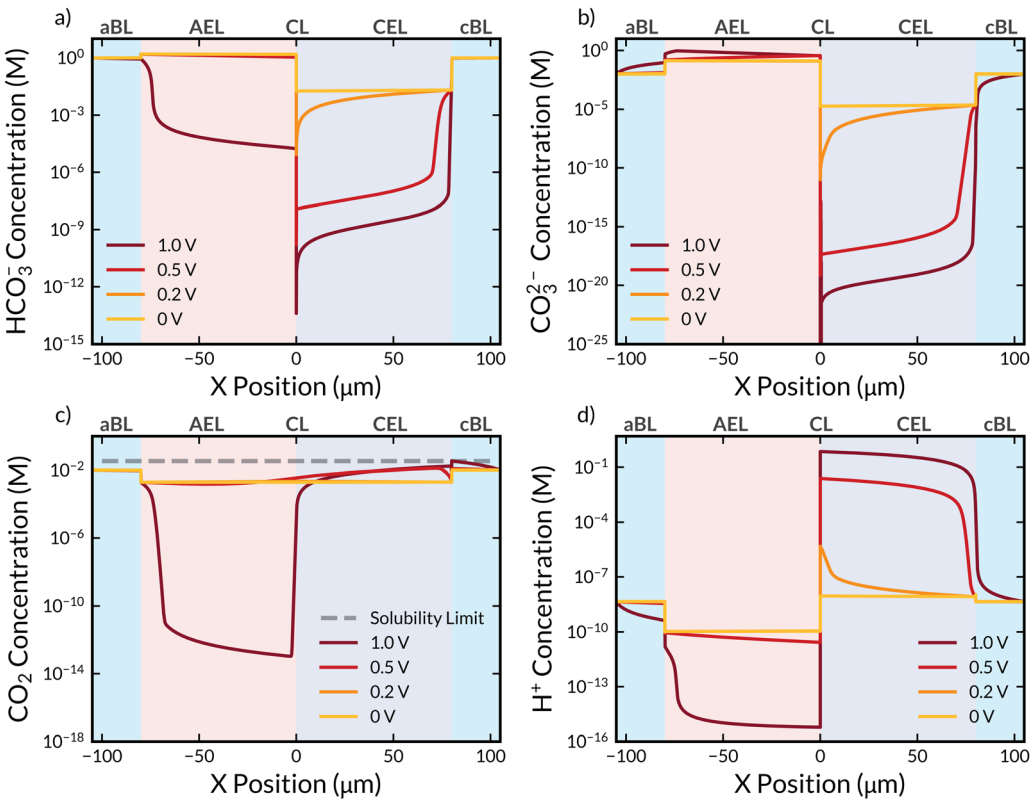

Fig. 4 Simulated concentration profiles of (a) HCO_3^-, (b) CO_3^{2-}, (c) dissolved CO_2, and (d) H^+ within a BPM immersed in 1 M $KHCO_3$ at applied membrane voltages of 0 V, 0.2 V, 0.5 V, and 1.0 V. Grey-dashed line in panel (c) denotes the solubility limit of CO_2 in water. Zoomed plots at the AEL|CEL interface can be found in Section S8 of the ESI.†

aqueous reactive carbon solutions. The simulated concentration profiles of HCO_3^-, CO_3^{2-}, CO_2, and H^+ within a BPM exchanged with 1 M $KHCO_3$ at applied potentials of 0 V, 0.2 V, 0.5 V, and 1.0 V, are shown in Fig. 4. Concentration profiles for OH^- as well as local pH can be found in Fig. S14 and S15 (ESI†). At equilibrium (0 V), both electrolyte boundary layers are fixed at their equilibrium concentrations for all species. Furthermore, within the BPM, there are no concentration gradients, and the concentrations are consistent with those determined by Donnan equilibrium within the interstitial pore volume.[27,45] Because of Donnan equilibrium with the catholyte, the CEL is fully exchanged with K^+ cations (Fig. S16 and S17, ESI†), and the AEL is fully exchanged with (bi)carbonates. Therefore, the pH in the CEL at equilibrium is near neutral, and that in the AEL is slightly alkaline (~pH 9) (Fig. S14b, ESI†).

As the applied potential increases, the pH within the CEL decreases significantly due to the generation of H^+ *via* water dissociation and bicarbonate dissociation. Consistent with the equilibria presented in eqn (1)–(5), as the pH in the CEL decreases, the concentrations of OH^-, CO_3^{2-}, and HCO_3^- decrease, and the concentration of CO_2 in the CEL increases. Additionally, diffusion gradients manifest in K^+ to maintain electroneutrality with the water-dissociation-generated H^+. Importantly, the model enables spatial resolution of *in situ* CO_2 regeneration, which is shown to occur only at the CEL|cBL interface, because the concentration of (bi)carbonates are too small within the CEL itself (due to Donnan exclusion) to facilitate reaction with water-dissociation-generated H^+. The H^+ from water dissociation exits out of the CEL and reacts with HCO_3^- in the electrolyte to form CO_2 that reaches its solubility limit, becomes saturated, and bubbles out, as is consistent with the experimental visual observation (Video S1, ESI†) and prior studies of BPMs operated in $KHCO_3$ solutions.[32,34]

On the AEL side, pH increases do not occur as readily with increasing cell potential, because the AEL is fully (bi)carbonate exchanged at equilibrium and the presence of (bi)carbonates in these high (~1–2 M) concentrations buffers changes in pH and pOH. This is important to note, because the pH gradient in these systems is typically assumed to be directly proportional to the electrostatic potential profiles (Fig. S22 and S23, ESI†).[58] However, these results demonstrate that the weak-acid buffer breaks the scaling relationship between the applied potential and the developed pH gradient by competitively consuming generated OH^- anions. Nonetheless, past potentials of 0.5 V, the pH does increase within the AEL. Past this potential, the concentration of dissolved CO_2 decreases significantly due to equilibrium reactions with water-dissociation-generated OH^- and is essentially entirely consumed within the AEL. Concurrently, HCO_3^- is consumed to form CO_3^{2-}, so the concentration of HCO_3^- in the AEL decreases, and that of CO_3^{2-} increases at high applied potentials. Once essentially all of the HCO_3^- in the AEL has been consumed ($V > 0.7$ V), the pH in the AEL increases much more rapidly, and the generated OH^- leaves the BPM and reacts with HCO_3^- anions in the anolyte. While the concentration of HCO_3^- in the AEL tends to zero at 1.0 V of applied potential, the HCO_3^- concentration in the vicinity of the AEL|aBL interface remains near the bulk concentration in the electrolyte, demonstrating that there is an abundance of reactive (bi)carbonate to consume water-dissociation-generated OH^- anions. It is important to note that while *in situ* CO_2 regeneration on the cathode side occurs only at the CEL|cBL interface due to exclusion of (bi)carbonates from the CEL, the regeneration of the CO_3^{2-} sorbent from the HCO_3^- occurs within the entirety of the AEL, CL, and anolyte domains. Because HCO_3^- can exchange (and is not excluded by Donnan equilibrium) into the AEL and CL, the direct field-enhanced dissociation of HCO_3^- anions in the CL, as well as the reaction of HCO_3^- with water-dissociation-generated OH^- throughout the CL, AEL, and anolyte, regenerate the CO_3^{2-} carbon capture sorbent.

A similar analysis of concentration profiles was also performed for BPMs immersed in simulated seawater (Fig. S18–S21, S24 and S25, ESI†). The model shows very similar behavior as for the 1 M $KHCO_3$ case with respect to the equilibria. However, due to the incredibly low concentrations of reactive carbon in the seawater electrolyte, the BPM is primarily exchanged with Na^+ or Cl^- for the CEL or AEL, respectively. At the CEL side, the catholyte is rapidly mass-transfer limited by HCO_3^-, impeding the formation of CO_2 *via* the *in situ* regeneration mechanism. However, on the AEL side, because there is a larger reactive volume of HCO_3^- wherein both the AEL and anolyte contain reactive HCO_3^-, the mass-transport limitations are less severe for the regeneration of the CO_3^{2-}, suggesting that the BPM-ED system for DOC is more effective for mineralization than for CO_2 release.

Lastly, because the equilibrium reactions are key to both the CO_2 and CO_3^{2-} regeneration, the ratio of the local forward and backward rates of each reaction (1)–(5), representing the deviation of these reactions from equilibrium, were plotted throughout the modeled domain for both the 1 M $KHCO_3$ and simulated seawater cases (Fig. S26–S29, ESI†). Interestingly, owing to their fast kinetics, reactions (1), (3) and (5) reach equilibrium throughout the entire domain, except for within the CL. However, reactions (2) and (4) significantly deviate from equilibrium within the catholyte where CO_2 regeneration occurs. Indeed, they favor their reverse direction, demonstrating that the water dissociation H^+ flux drives these reactions out of equilibrium towards regenerating CO_2. This analysis demonstrates the importance of the BPM pH swing in driving buffer reactions.

3.3. Simulated fluxes and transference numbers of ionic species

While an understanding of the local concentrations and environments within the BPM provides valuable information regarding the phenomena occurring within it, knowledge of the fluxes of the various ionic species in these membranes is just as crucial. The primary charge carrier within an ion-exchange membrane dictates its conductivity,[51,54,59] and understanding charge transport through the BPM is key to mitigating detrimental phenomena such as salt crossover.[27] Plotting the effective transference numbers, defined here as the fraction of current carried by a given species, of all ions as a function of applied potential

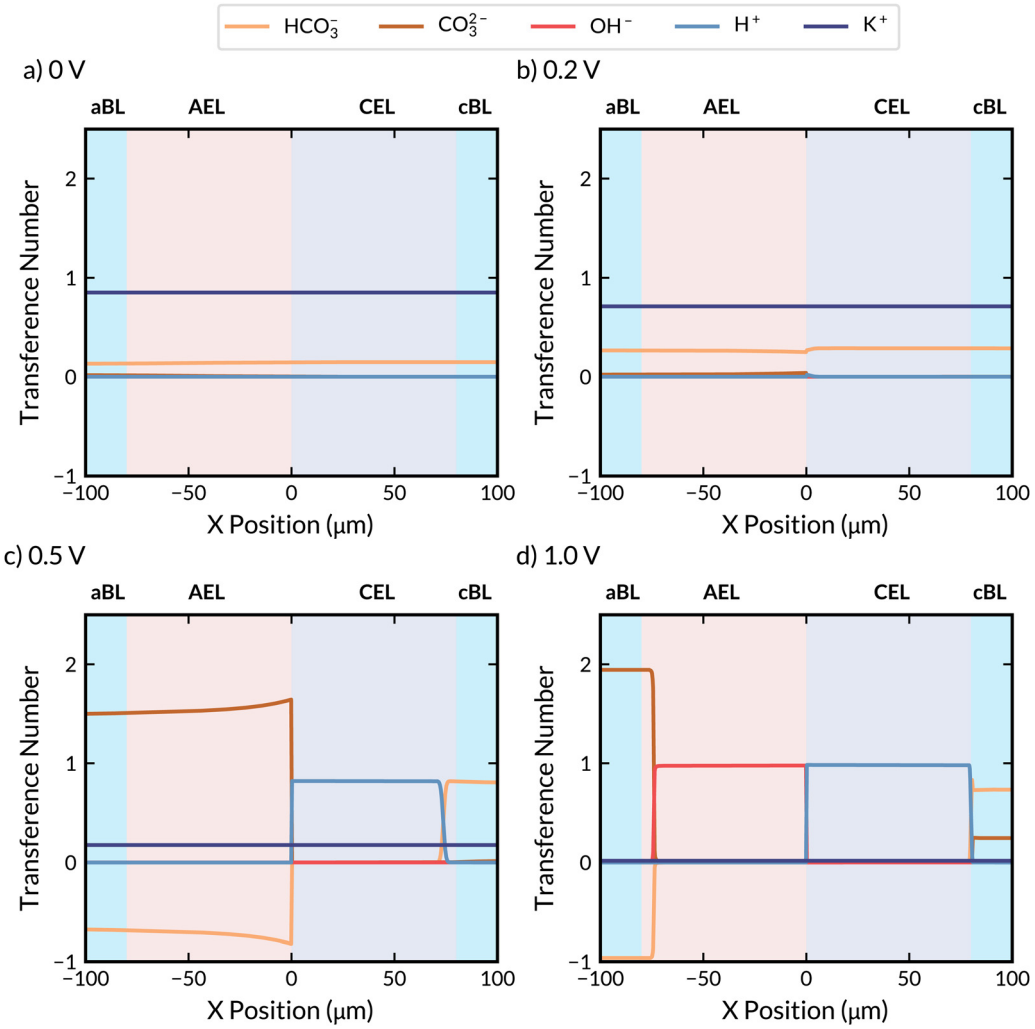

Fig. 5 Simulated effective transference-number profiles of HCO_3^-, CO_3^{2-}, H^+, OH^-, and K^+ within a BPM immersed in 1 M $KHCO_3$ at applied membrane voltages of (a) 0 V, (b) 0.2 V, (c) 0.5 V, and (d) 1.0 V.

throughout the BPM (Fig. 5 and Fig. S30–S32, ESI†) reveals the nature of charge transport within the BPM operated with 1 M $KHCO_3$. At low applied potentials (0 V and 0.2 V), the current density is primarily due to co-ion crossover (Fig. 5a and b) (K^+ crossing from the anolyte to catholyte or HCO_3^- crossing from the catholyte to anolyte), with K^+ the dominant carrier of current, due to its higher diffusion coefficient in the BPM.[27]

As the applied potential is increased and electric-field-enhanced water dissociation occurs, H^+ rapidly becomes the primary charge carrier in the CEL (Fig. 5c and d). For the AEL, on the other hand, CO_3^{2-} becomes the primary charge carrier at moderate potentials (0.4–0.7 V), and HCO_3^- possesses a negative effective transference number (Fig. 5c). This flux behavior is consistent with the interpretation that HCO_3^- transports as a counter-ion through the AEL to the CL, where it is either directly dissociated by the large electric field or reacts with water-dissociation-generated OH^- to form CO_3^{2-} that can then transports directly out of the CL and serves as the major carrier of charge in the AEL. At higher potentials (>0.7 V), where HCO_3^- is depleted, OH^- becomes the primary charge carrier in the AEL (Fig. 5d). Interestingly, H^+ and OH^- do not immediately become the primary carrier of charge in the BPM when water dissociation begins at $\sim$0.5 V, and there appears to be a penetration depth moving out from the CL through which the fronts of H^+ and OH^- flux dominate. This penetration depth is dependent on the current density and is due to out-of-equilibrium buffer reactions that convert the generated OH^- or H^+ to alternative charge carrying ions within the BPM domain. At large enough current densities, the buffering species within the BPM are depleted, and H^+ and OH^- become the dominant charge carriers throughout the entirety of the BPM. This flux analysis was also carried out for the simulated seawater case and similar trends were observed (Fig. S33–S35, ESI†). However, due to the small concentration of reactive carbon in the seawater, OH^- and H^+ more rapidly become the primary charge carriers in the BPM.

Taken together, this knowledge suggests that operation of BPM-ED systems at high current density could be beneficial for several reasons. At higher current densities, salt crossover is less extensive due to the dominance of H^+ and OH^- as charge

carriers. Additionally, at these higher current densities, OH^- fully replaces the initially exchanged (bi)carbonates as the charge carrying species in the AEL, which reduces ohmic losses due to the higher mobility of OH^-.[60]

3.4. Energy intensities and efficiency of CO_2 desorption *via* BPM-ED

Key to any carbon-capture process is understanding the efficiency and energy requirements for operation at various rates. One key promise of EMCC processes is that they could potentially enable lower energy intensities than thermal processes.[2] Thus, the simulation was employed to determine the coulombic efficiency of CO_2 regeneration (Fig. 6a) and energy intensity (Fig. 6b) for CO_2 regeneration as a function of applied current density. Coulombic efficiency is defined as the fraction of the applied current density that goes toward regenerating CO_2 and can be thought of as the product of the water dissociation efficiency, and the efficiency of reacting water-dissociation-generated H^+ with HCO_3^- to form CO_2.

For all electrolytes tested (0.5 M $KHCO_3$, 1 M $KHCO_3$, and simulated seawater), the coulombic efficiency initially is 0% due to the dominance of salt-crossover at low current densities. Nonetheless, the efficiency rapidly increases to ~80% for all electrolytes due to the onset of the water dissociation reaction. Crucially, water dissociation in all electrolytes rapidly reaches ~99% efficiency (Fig. S36, ESI†), consistent with prior study of the Fumasep BPM, meaning that deviations in coulombic efficiencies lower than 99% are due to inefficiencies in conversion of the generated H^+.[40]

The coulombic efficiency (Fig. 6a, orange trace) for DOC by BPM-ED from simulated seawater monotonically decreases as the current density increases. The rapid decrease of coulombic efficiency for simulated seawater is due to complete consumption of the dilute 0.00211 M HCO_3^- in the catholyte (*i.e.*, the CO_2 regeneration is HCO_3^- limited). Once all the HCO_3^- in the cBL is consumed, the H^+ flux from the BPM exits the cBL unreacted, acidifying the bulk electrolyte. The impact of unreacted H^+ can be seen due to the effective transference number of H^+ in the catholyte reaching 1 at high current densities (Fig. S33, ESI†), meaning that the majority of the current density goes towards acid generation. Importantly, while the Na^+ and Cl^- present in seawater contribute to the ionic strength of the solution they do not participate in buffer reactions, and therefore the presence of these ions does not impact the rate of field-enhanced water and bicarbonate dissociation in the BPM. Co-ion crossover reduces efficiency. However, the crossover of co-ions contributes < 2% of coulombic efficiency at current densities beyond 5 mA cm^{-2}, suggesting that the presence of these ions does not substantially impact performance for BPM-ED. It is important to note that the coulombic efficiency defined herein is the coulombic efficiency of H^+ liberating CO_2 within the diffusion boundary layer. Unreacted H^+ could theoretically react with further dissolved inorganic carbon to liberate greater amounts of CO_2 by feeding more electrolyte downstream. However, in this work, we seek to consider just the fluxes in the direct vicinity of the BPM to explore the effects of mass transfer at the micrometer scale. This effect may vary near the terminal electrodes in a BPM-ED stack depending on the consumption of protons and hydroxides by the redox reactions.

For the 0.5 M and 1 M $KHCO_3$ electrolytes relevant to DAC, the coulombic efficiency (Fig. 6a, red and blue traces) similarly decreases after achieving a maximum of ~80%. However, instead of being HCO_3^- limited, the reduction in coulombic efficiency at intermediate current densities is limited by the consumption of H^+ by CO_3^{2-} to form HCO_3^- (Fig. S38, S39 and Section S17, ESI†). Once all of the CO_3^{2-} in the catholyte has been consumed, there is an inflection point in the coulombic efficiency at which the CO_2 regeneration increases again, achieving higher coulombic efficiencies approaching 90% for 1 M $KHCO_3$ and 95% for 0.5 M $KHCO_3$ at current densities approaching 100 mA cm^{-2}. The coulombic efficiencies reported in these electrolytes are also consistent with prior work by Eisaman *et al.*[16] Between 0.5 and 1 M $KHCO_3$, 0.5 M $KHCO_3$ possesses a higher coulombic efficiency at high current density due to its lower bulk pH, which inhibits the loss of water dissociation generated H^+ to H^+–OH^- recombination and H^+–CO_3^{2-} recombination relative to the 1 M $KHCO_3$ case.

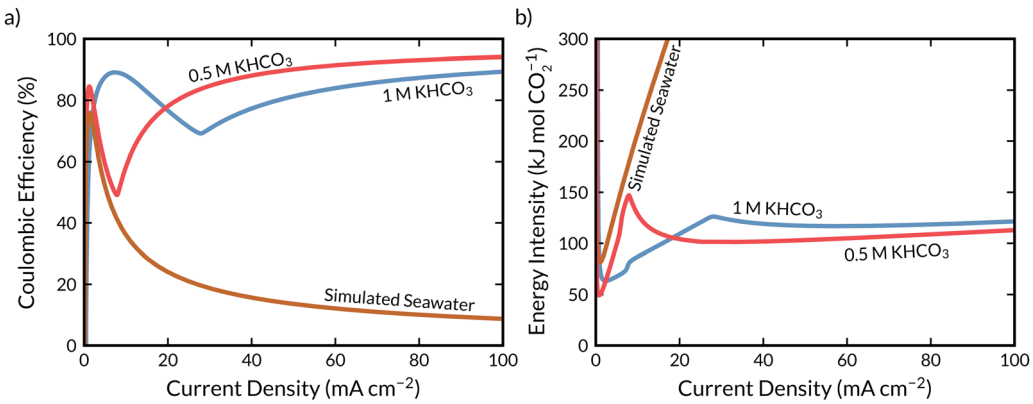

Fig. 6 Simulated (a) coulombic efficiency and (b) energy intensity of BPM-ED for EMCC from 1 M and 0.5 M $KHCO_3$ as well as for DOC in simulated seawater.

Considering the energy intensity for these processes, the simulated seawater BPM (DOC) possesses higher energy intensity (Fig. 6b, orange trace) at high current densities due to mass-transport limitations associated with the low concentrations of dissolved carbon species and the resulting low coulombic efficiency. However, at low current densities, where the flux is well matched to the concentration of (bi)carbonates, the energy intensity for CO_2 generation by the BPM is <100 kJ mol CO_2^{-1}. Further, the simulated energy intensity for CO_2 desorption at 3.3 mA cm^{-2} is 108 kJ mol CO_2^{-1}, which agrees quite well with the 155 kJ mol CO_2^{-1} experimentally reported by Digdaya *et al.*,[7] when considering the energy requirement in that report included losses associated with a ferro/ferricyanide redox couple at the working and counter electrodes ($\sim$40 kJ mol CO_2^{-1} at an equivalent current density).

Conversely, the 1 and 0.5 M $KHCO_3$ cases (DAC) require lower energy intensities (Fig. 6b, red and blue traces) due to higher concentrations of HCO_3^- anions in the catholyte boundary layer for reaction, maintaining energy intensities near 100 kJ mol CO_2^{-1} even at current densities of 100 mA cm^{-2}. 0.5 M $KHCO_3$ possesses a lower energy intensity due to its higher coulombic efficiency at high current densities. These energy intensities compare well with thermal processes, and the current densities achieved far exceed those demonstrated for other EMCC processes.[2,23]

The coulombic efficiency of sorbent regeneration in the AEL is nearly 100% in the $KHCO_3$ solutions tested for DAC (Fig. S40 and S41, ESI†). This is likely due to an increased space time for HCO_3^- conversion into CO_3^{2-}. The ability of the AEL to exchange with both HCO_3^- and water-dissociation-generated OH^- enables a high activity for these ions to react and form CO_3^{2-} in the anolyte boundary layer and within the AEL and CL. For DOC, the buffer reactions in the simulated seawater BPM are still limited by HCO_3^- concentration, but the conversion efficiency for sorbent regeneration is higher than that of CO_2 recovery again due to increased space time, maintaining a value $>30\%$ at all current densities (Fig. S40 and S41, ESI†).

Lastly, we note that a BPM with $KHCO_3$ electrolytes implemented in a DAC loop as shown in Fig. 1a, will likely operate with a gradient in pH and dissolved carbon species, as the electrolyte fed back to anolyte side will be slightly acidified and have some carbon removed. Thus, the simulation was run with a gradient across the BPM in both pH and dissolved inorganic carbon, wherein the catholyte was fed with 1 M $KHCO_3$ (pH = 8.3) as before, but the anolyte was fed with 0.9 M $KHCO_3$ (pH = 7.5) to represent 10% stripping of carbon by BPM-ED and the following CO_2 stripping process. As shown in Fig. S42 and S43 (ESI†), the choice to operate under this gradient has no effect on the energetics or efficiency for CO_2/CO_3^{2-} recovery, except at very low current densities ($i <$ 10 mA cm^{-2}) due to a large diffusive flux at 0 V associated with the imposed concentration gradient across the BPM. All told, the high coulombic efficiencies and low energy intensities (competitive with thermal desorption)[5] demonstrated indicate that BPM-ED possesses promise for application as a carbon-removal technique.

Collectively, the above analysis demonstrates that regeneration of CO_2 and in BPM-ED EMCC is dictated by complex interactions between H^+, HCO_3^-, and CO_3^{2-} *via* their associated buffer kinetics. Additionally, the results demonstrate that while DOC systems do not need to employ air contactors, they rapidly become mass transport limited at current densities beyond 10 mA cm^{-2}, where coulombic efficiency becomes dominated by acid or base generation rather than CO_2 recovery. Consequently, a potential approach is to simply generate acid and base from seawater *via* BPM-ED at elevated current densities and use the generated acid and base for oceanwater acidification or mineralization in downstream chemical reactors.[61] Conversely, $KHCO_3$ electrolytes used in DAC enable high coulombic efficiencies and low energy intensities even at current densities exceeding 100 mA cm^{-2} and may be more suitable for direct EMCC looping. The trends observed for the CO_2 recovery energy intensity between 1 M $KHCO_3$, 0.5 M $KHCO_3$, and simulated seawater suggest a trade-off with regard to the electrolyte composition. Reducing the buffer capacity of the carbon capture solution will improve performance by enabling more facile pH swings and CO_2 recovery. However, extremely low contents of the buffer will incur mass transfer limitations that increase energy intensity. Nonetheless, a full technoeconomic analysis is necessary to weigh the economic advantages of each system but is beyond the scope of the present work.

3.5. Effect of CO_2 bubble formation on BPM-ED performance

Management of bubbles is key in the development of electrochemical devices,[56,62,63] and this is especially true for carbon-capture devices that must mediate the generation of CO_2 gas from an aqueous (bi)carbonate electrolyte. Work by Diederichsen *et al.* identified bubble management as a key challenge in continuous EMCC systems due to power losses that occur from loss of electrochemically active surface area due to CO_2 bubbling.[12] The model presented here enables a simulation of the bubble coverage on the CEL, as well as an understanding of how the bubble coverage affects the energy requirements for BPM-ED EMCC.

First, it is important to note that due to mass-transport limitations in the seawater case as discussed above, bubbling only occurs for the BPMs exchanged with $KHCO_3$. Analysis of the bubble coverage in these simulations (Fig. 7a) shows that the bubble coverage of the BPM exceeds 30% at high current densities due to super saturation of the electrolyte. This high bubble coverage is consistent with visual observation of the CEL during operation (Video S1, ESI†). Additionally, the analysis of the energy requirements with and without losses due to bubble coverage reveals that bubble effects account for nearly 10 kJ mol^{-1} of energy loss (Fig. 7b) for both $KHCO_3$ cases at 100 mA cm^{-2}. Therefore, managing bubbles is indeed crucial to improving energy efficiencies for BPM-ED EMCC. Previous knowledge from water electrolysis shows that bubble coverage losses can be ameliorated by controlling flow rate,[64] or by employing a surfactant to reduce surface tension and bubble size.[65,66] The BPM morphology and surface chemistry can also be modulated to alter the wettability and coverage of bubbles on the surface. Finally, pressurizing the bicarbonate solution can improve CO_2 solubility,[64,67] which not only mitigates

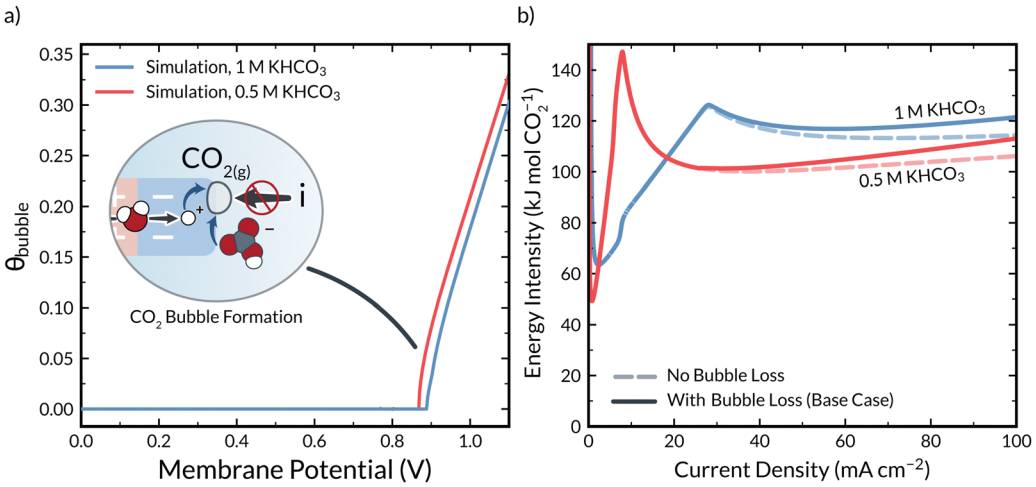

Fig. 7 Effect of CO_2 bubble formation on energetic penalties in BPM-ED EMCC. (a) Simulated bubble coverage as a function of applied membrane potential. (b) Simulated energy intensity of a BPM with no bubble management (solid lines) and perfect bubble management (dashed lines).

bubble formation but also enables generation of the CO_2 at higher pressures which ultimately reduces downstream compression costs required for CO_2 transportation and sequestration as shown by previous analysis of EMCC processes.[18] Bubble formation will also be impacted by increases in temperature, which reduce CO_2 solubility according to Henry's Law and further exacerbates bubble formation. This phenomenon has been shown in bicarbonate electrolyzers, where higher CO_2 generation rates were observed at higher electrolyte temperatures.[67]

The effect of flow rate can be represented in our model through the thickness of the anolyte and catholyte diffusion boundary layers. Lower flow rates are represented by thicker boundary layers, and higher flow rates are represented by thinner boundary layers.[68] As shown in Fig. S44 and S45 (ESI†), changing the flow rate has little effect on the polarization curve when deconvoluting bubble induced surface area losses (*i.e.*, flow rate has no impact on the base BPM energy requirement) or the overall rate of CO_2 flux from the catholyte. However, increasing flowrate does increase the onset current density for which bubbling is observed, reducing bubble coverage. At the base case boundary-layer thickness of 25 μm (corresponding to a Reynolds number (Re) of 18 000, which is in the laminar flow regime over a smooth flat plate[69]), bubbling occurs at a current density of approximately 20 mA cm^{-2}, consistent with experiment. However, for a boundary-layer thickness of 10 μm (corresponding to Re of 111 000, still in the laminar flow regime for a flat plate[69]), bubbling does not occur until 60 mA cm^{-2}. The delay on the onset of bubbling occurs because the faster transport of CO_2 away from the reactive CEL|cBL boundary prevents supersaturation and keeps CO_2 dissolved within the aqueous electrolyte.

To highlight the importance of bubble management, further experiments were performed. In these studies, the BPM-ED system was run with various electrolyte flowrates, and the extent of CO_2 bubbling was quantified by determining the noise in the measured electrostatic potential as calculated by the standard deviation in the measured transmembrane potential (details on these experiments can be found in Section S21, ESI†). Fig. S47a (ESI†) compares standard deviation of potential as a function of applied current density for three different flow rates (0.2, 1, and 5 mL min^{-1}). As shown in the figure, the extent of bubbling is much more severe for lower flowrates, and the onset of bubbling occurs at lower current densities, as predicted from the model.

Fig. S48a and b (ESI†) depict polarization curves for Fumasep tested at each flow rate in 1 M $KHCO_3$ and 0.5 M NaCl, respectively. Comparing the two plots indicates that the addition of bicarbonate species into the electrolyte increases the average voltage measured at each current density. Furthermore, without the bicarbonate species present (Fig. S48b, ESI†), flowrate has no effect of the measured BPM voltage, signifying that flowrate dependence is only introduced once the bicarbonate is added to induce CO_2 bubble formation, in agreement with the simulations. Indeed, in the presence of bicarbonate (Fig. S48a, ESI†), the average voltage is highest for the lowest flowrate, indicating that an increase in bubble coverage under reduced flows leads to decreased surface area and increased resistance. This experimental data further supports the importance of flowrate and bubble mitigation on maintaining low cell voltages when operating BPMs for carbon removal due to the surface area losses driven by CO_2 bubble formation on membrane surfaces.

3.6. Impact of divalent cations on DOC performance

BPMs applied to DOC will also have to contend with the presence of divalent cations in oceanwater (Table S4, ESI†). Namely, Mg^{2+} and Ca^{2+} appear in concentrations of 53 and 10 mM, respectively in naturally-occurring oceanwaters.[70] These contaminants can lead to precipitation of $Ca(OH)_2$ or $Mg(OH)_2$ on the BPM surface, which is a major failure mode of BPMs operating in real process waters.[71] These ions also impact performance and durability at the terminal electrodes (Section S23.1, ESI†). Hence, understanding the impacts and concentrations of divalent cations in BPMs for DOC will be key to advancing the technology. Simulations were run wherein divalent cations were included in the aqueous

electrolyte to observe their impacts on the BPM performance and local environments. As can be seen from Fig. S50 (ESI†), the presence of divalent cations has very little effect on the polarization behavior of the BPM, increasing the required membrane potential to achieve a given current density only slightly. This minimal increase in the required overpotential results from a slight reduction in the local electric field within the BPM junction upon introduction of Mg^{2+} and Ca^{2+} that slightly reduces the electric-field enhanced water dissociation rate (Fig. S51, ESI†). Additionally, it can be seen that these divalent cations do not carry significant current density, with Ca^{2+} and Mg^{2+} carrying at most 3 and 13% of the current, respectively, and both approach 0% transference at high current densities (Fig. S52, ESI†). The presence of these ions also does not impact trends in carbon concentration and pH profiles (Fig. S53, ESI†). However, it is important to note that due to their divalent charge, these cations partition strongly into the CEL *via* Donnan equilibrium, with the Mg^{2+} and Ca^{2+} possessing concentrations of 0.5 and 0.09 M, respectively, in the CEL of the BPM (Fig. S54, ESI†). These high concentrations of divalent cations in the CEL can explain the precipitation of salts observed in BPM systems with real process waters.[71] Hence, systems for BPM-ED with Ca^{2+} or Mg^{2+} containing process streams should seek to mitigate divalent cation absorption in the CEL. Berlinguette and co-workers have achieved this through the addition of a thin polyaniline layer on the outside of the CEL that electrostatically excludes divalent cations from entering the CEL.[71] Divalent cations can also be removed from seawater prior to BPM-ED *via* nanofilitration or Donnan dialysis.[72,73] However, additional research will be required to fully develop and characterize systems that enable selective rejection of divalent contaminants in BPMs for EMCC.

3.7. Applied-voltage-breakdown analysis for BPM-ED EMCC

Because knowledge of the energetic requirements for BPM-ED EMCC is critical to the optimization and implementation of these systems, voltage contribution analysis[74] of the BPM operating in 1 M $KHCO_3$ and simulated seawater were conducted to determine the major sources of power loss in the BPM-ED system. As expected for both the DOC and DAC solutions, the thermodynamic potential required to drive the pH gradient across the CL (Section S1.2, ESI†) makes up the largest contribution to the applied potential. This thermodynamic potential is equivalent to the pH difference across the AEL|CEL interface, and is approximately 0.83 V ($0.059 \times pK_w$) for water dissociation, and 0.60 V ($0.059 \times pK_{a,HCO_3^-}$) for bicarbonate dissociation. In the bicarbonate dissociation regime, the thermodynamic potential is equal to thermodynamic potential for bicarbonate dissociation, and in the water dissociation regime, the thermodynamic potential is equal to the thermodynamic potential for water dissociation, as labeled in Fig. 8. These thermodynamic potentials are shifted by the sum of Donnan potentials at the aBL|AEL and CEL|cBL interfaces[75] (dashed lines in Fig. 8, see Fig. S22 (ESI†) for visualization of Donnan potentials). This shift due to the Donnan potential at each interface facilitates WD at external membrane voltages of <0.83 V, because these Donnan potentials ensure that the potential at the AEL|CEL interface where the WD reaction occurs is ~ 0.10 V larger than the voltage applied across the BPM externally. These thermodynamic phenomena explain

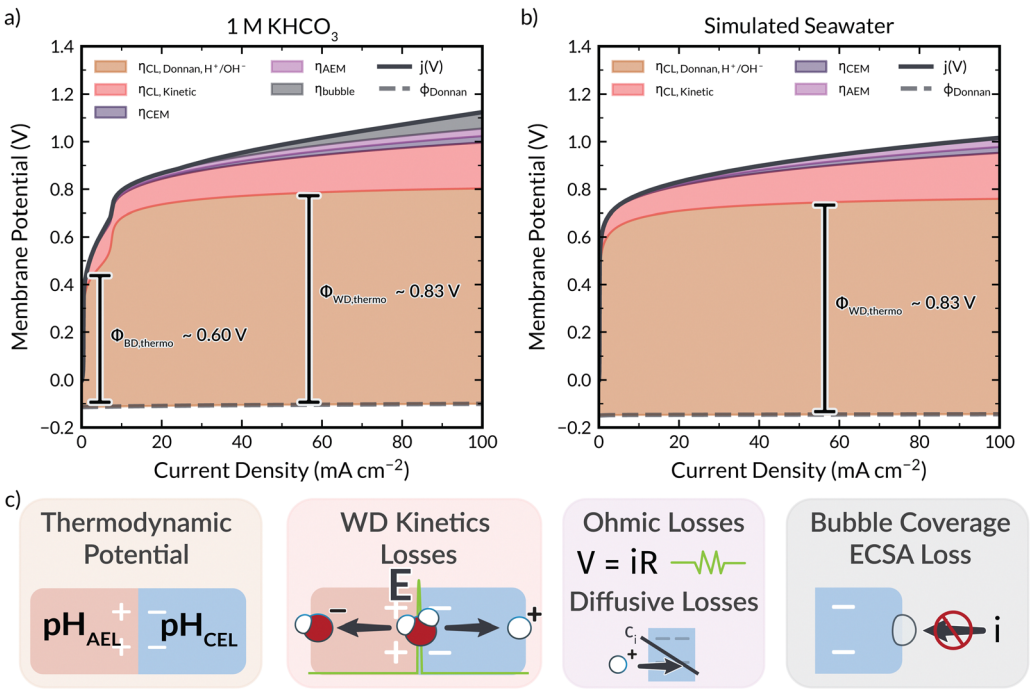

Fig. 8 Applied-voltage breakdown for a BPM immersed in (a) 1 M $KHCO_3$ and (b) simulated seawater. Dashed lines represent the shift in the BPM potential associated with Donnan potentials at the aBL|AEL and CEL|cBL interfaces (see Fig. S22, ESI†). Brackets in the thermodynamic potential represent the thermodynamic potentials associated with bicarbonate dissociation (BD) and water dissociation (WD). (c) Schematic depictions of various voltage loss mechanisms.

how many reports observe meaningful WD rates at applied potentials <0.83 V.[53,76]

The next largest potential loss in both systems is the kinetic overpotential for the water dissociation in the CL (Section S1.2, ESI†). While the thermodynamic requirements cannot be altered, the kinetic overpotential can be lowered by employing a better water-dissociation catalyst.[26,42] For the 1 M $KHCO_3$ case, bubble coverage losses also make up a significant portion of the applied potential, particularly at high current densities, and those could be managed by better controlling the flow of electrolyte, as discussed in Section 3.5, or through other bubble-mitigation strategies. Bubble formation does not occur in DOC systems due to low carbon concentrations as discussed in Section 3.5. Lastly, ohmic and diffusive losses (Section S1.7, ESI†) through the CEL and AEL are quite low relative to other losses but do increase with current density and will likely become critical if the BPM-ED system is to operate at currents approaching 1 A cm^{-2}. Although minor, these losses can be decreased by improving ionic conductivity of the AEL and CEL. This applied-voltage breakdown highlights that the greatest areas for improvement in the BPM-ED performance are in improving the water dissociation catalyst and in implementing bubble-management strategies in the case of DAC.

3.8. Sensitivity analysis of BPM-ED EMCC

Sensitivity analysis was performed on the BPM-ED simulations to better understand the effect of BPM and CL properties on the performance of the BPMs immersed in reactive carbon solutions. For the following sensitivity analyses, the effects of bubble coverage are not considered, essentially assuming that a bubble mitigation strategy has been developed and implemented. Prior studies have demonstrated that the increase of the ion-exchange capacity (IEC) or fixed-charge in the BPM can enhance the rate of water dissociation by increasing the electric field between the AEL and CEL.[26,50] As shown in Fig. S55 and S56 (ESI†), increasing the IEC does indeed improve the rate of water dissociation significantly, and consequently the rate of CO_2 flux at a given applied potential. Improving the performance of the water-dissociation catalyst has also been proven to be key in reducing energy requirements for BPM operation.[42,77] As such, the model was run with varying values of α_{WD}, which represents the sensitivity of water dissociation to the electric field. The results show that performance of the BPM in reactive carbon solutions is indeed incredibly sensitive to the catalyst activity (Fig. S57, ESI†). Sensitivity analysis was also performed to discern the impact of membrane thickness and water uptake (Section S24.1, ESI†). Taken together, these results indicate that the greatest potential for BPM improvement lies in enhancing bubble removal from the BPM surface, increasing the IEC of the ionomers, and using a better WD catalyst to enhance the performance of BPM-ED EMCC.

Recent work by Pintauro *et al.* demonstrated a BPM meeting these criteria, employing a BPM with a high fixed-charge concentration and a complex 3-D junction CL for efficient water dissociation in a 0.5 M Na_2SO_4 electrolyte.[76] This BPM differs from the Fumasep due to its higher fixed-charge density ($\sim 2\times$ that of Fumasep), as well as its electrospun 3-D junction $Al(OH)_3$ water dissociation catalyst that exhibits improved kinetics over the proprietary catalyst employed by Fumasep. Parameters in the model were fit in order for the simulation to match observed performance by Pintauro in 0.5 M Na_2SO_4 (Section S24.2, ESI†) and the performance of the "Optimal BPM" in reactive carbon capture solutions was simulated. As shown in Fig. 9a, employing the optimal BPM dramatically improves the polarization behavior compared to the Fumasep BPM for both DAC and DOC applications. More promising, however, is recognition that the use of the Optimal BPM substantially lowers the energy intensity for CO_2 desorption well below 100 kJ mol CO_2^{-1}, even at current densities at or exceeding 100 mA cm^{-2} for the 0.5 and 1 M $KHCO_3$ electrolytes (Fig. 9b). For DOC applications, the optimized BPM does indeed lower energy intensities, but the system is still mass transport limited for CO_2 and sorbent regeneration. Nonetheless, the improvements in BPM performance facilitate higher rates of acid and base generation from oceanwater at reduced potentials. Applied-voltage breakdowns (Fig. S63, ESI†) demonstrate that these improvements are due to improved ionic conductivity due to the enhanced IEC, as well as significantly

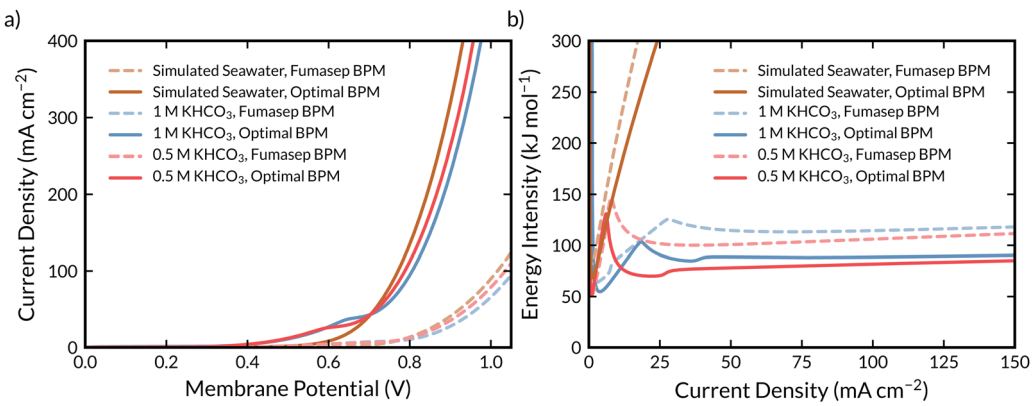

Fig. 9 Sensitivity analysis of BPM polarization curves in various EMCC solutions. (a) Sensitivity of polarization curve to BPM properties. (b) Sensitivity of energy intensity to BPM properties.

reduced overpotentials for water dissociation due to the high IEC and improved catalytic behavior, along with the assumed mitigation of bubble losses in the system.

The above calculations correspond to the energy intensity of a single BPM unit in an overall stack, and the number of BPMs in the stack will be key to dictating efficiency, especially when considering the electrode potentials of the anode and cathode. As shown in Fig. S64 (ESI†), considering the effect of the anode and cathode potentials does increase the energy intensity of the process quite significantly (from 88 kJ mol CO_2^{-1} to 176 kJ mol CO_2^{-1} at 100 mA cm^{-2}) for a DAC system employing a 1 M $KHCO_3$ capture solution. However, as the number of BPMs in the stack increases, the energy intensity rapidly approaches that of the single BPM unit simulated herein. For a BPM-ED stack containing ten of the Optimal BPMs, the theoretical energy intensity is still below 100 kJ mol CO_2^{-1} at 100 mA cm^{-2} (see Section S25, ESI† for the details of this calculation). Ultimately, this analysis reveals the exciting result that newly developed BPMs have achieved such substantial strides in water-dissociation catalysis that CO_2 desorption *via* BPM-ED could be achieved at energy intensities lower than 100 kJ mol CO_2^{-1} even for current densities exceeding 100 mA cm^{-2}, making this technology quite promising for carbon removal when considered in a BPM-ED stack configuration.

4. Conclusions

Electrochemically mediated carbon capture strategies have the potential to displace thermal desorption techniques due to their ability to operate with lower energy requirements at ambient temperatures and pressure. Bipolar-membrane electrodialysis (BPM-ED) is a promising technique that uses the H^+ and OH^- fluxes generated by electric-field-enhanced water dissociation in a BPM to drive the release of CO_2 and the recovery of CO_3^{2-} from an electrolyte containing reactive carbon species simultaneously. Herein, we developed simulations, which closely match experiments, and resolved the rates of the various kinetic and transport processes (field enhanced water or bicarbonate dissociation, homogeneous buffer reactions, salt crossover, *etc.*) occurring within BPMs immersed in three reactive carbon solutions relevant to carbon capture: 1 M $KHCO_3$, 0.5 M $KHCO_3$, and simulated seawater. Simulations reveal that an early onset in observed current density for (bi)carbonate exchanged BPMs is due to field enhanced dissociation of the bicarbonate anions as well as a reduction in H^+-OH^- recombination due to competitive reaction of OH^- with HCO_3^- to form CO_3^{2-} indirectly.

Local concentrations and fluxes in the BPM from the simulations elucidated that alkali cations and (bi)carbonates are the dominant ion and primary charge carrier in the BPM at low current densities, with water-dissociation generated H^+ and OH^- becoming the dominant ions at high current densities once buffering (bi)carbonate anions are consumed by homogeneous reaction. The energy intensity for CO_2 desorption as a function of applied current density was also determined. The model reveals that the low concentration of (bi)carbonates in simulated seawater leads to mass-transport limitations and consequently high energy intensities for CO_2 recovery at elevated current densities for BPMs applied for DOC. This suggests that high-current-density BPM-ED in seawater should aim to produce acid and base that can be used in carbon removal processes downstream. Conversely, BPMs in higher concentrations of (bi)carbonates do not become mass-transport limited for CO_2 recovery up to 100 mA cm^{-2} and can achieve energy intensities competitive with thermal desorption of approximately 100 kJ mol^{-1} at current densities far exceeding those demonstrated for other EMCC processes. Collectively, these results reveal that reducing the buffer capacity of the carbon capture solution reduces energy intensity by enabling facile pH swings, but that at extremely low contents of carbon in the electrolyte, mass transfer limitations occur that increase energy intensity. Correspondingly, future work should seek to explore the impact of electrolyte composition in more detail to find the optimum of this tradeoff. Lastly, analysis of the losses in the DAC system revealed that the greatest opportunities for optimization of these systems are through the management of CO_2 bubbles and the improvement of the water-dissociation performance. Simulating a BPM with bubble-mitigation strategies, greater ion-exchange capacity, and a substantially enhanced water dissociation catalyst (consistent with the state-of-the-art BPM in literature) shows that these improvements enable performance for BPM-ED EMCC at 100 mA cm^{-2} at energy intensities well below 100 kJ mol CO_2^{-1}.

Future work should aim to employ technoeconomic analysis to weigh the pros and cons of BPM-ED for DAC with concentrated bicarbonates *versus* DOC with oceanwater. Furthermore, detailed modeling and analysis of degradation mechanisms, such as precipitation of divalent contaminants, spontaneous delamination, and chemical degradation *via* radical attack or oxidative instabilities, will be required to truly advance the technology to industrial relevance. Nonetheless, this work provides substantial insight into the mechanistic behavior of reactive carbon species in BPM systems, relevant to many electrochemical systems across the gamut of carbon-capture and -conversion technologies and elucidates the promise of BPMs in performing BPM-ED for carbon capture at current densities exceeding 100 mA cm^{-2}.

Nomenclature

Roman

a_i	Activity of species i
c_i	Concentration of species i (M)
D_i	Diffusivity of species i (m^2 s^{-1})
E	Electric field (V m^{-1})
f_i	Activity coefficient of species i
F	Faraday constant (C mol^{-1})
G	Gibbs free energy (J mol^{-1})
IEC	Ion exchange capacity (mmol g^{-1})
k_B	Boltzmann constant (J K^{-1})
K_n	Equilibrium constant in reaction n
k_n	Forward rate constant of reaction n (mol m^{-3} s^{-1})

L	Length (m)
l_B	Bjerrum length (m)
M_i	Molar mass of species i (g mol^{-1})
N_i	Molar flux of species i (mol m^{-2} s^{-1})
R	Ideal gas constant (J mol^{-1} K^{-1})
$R_{B,i}$	Source term for species i (mol m^{-3} s^{-1})
$s_{i,n}$	Stoichiometric coefficient of species i in reaction n
T	Temperature (K)
x	1-dimensional position variable (m)
z_i	Charge of ion i

Greek

β	Non-dimensional electric field scaling factor (m V^{-1})
ε	Dielectric permittivity (F m^{-1})
λ	Water content
μ	Chemical potential of species i (J mol^{-1})
ξ	Species-membrane/species-water diffusivity ratio
ρ	Density (g cm^{-3})
σ	Dimensionless dissociation bond length
ϕ	Electrostatic potential (V)
ε_k	Volume fraction of phase k

Subscript

char	Characteristic
eff	Effective
i	Species index
M	Value in membrane
w	Value in water

Superscript

0	Intrinsic value or standard state
E	Electric field dependence

Acronyms

aBL	Anolyte boundary layer
AEL	Anion exchange layer
BPM	Bipolar membrane
BPM-ED	Bipolar membrane electrodialysis
cBL	Catholyte boundary layer
CEL	Cation exchange layer
CL	Catalyst layer
EMCC	Electrochemically-mediated carbon capture
WD	Water dissociation

Conflicts of interest

Three of the authors, Éowyn Lucas, Harry A. Atwater and CX Xiang, are stockholders of the company Captura Corporation, which has taken an option to license intellectual property from Caltech related to direct ocean capture with bipolar membranes.

Acknowledgements

This material is based on work performed within the Liquid Sunlight Alliance, which is supported by the U.S. Department of Energy, Office of Science, Office of Basic Energy Sciences, Fuels from Sunlight Hub under Award Number DE-SC0021266. JCB would like to acknowledge support from the National Defense Science and Engineering Graduate Fellowship (NDSEG) supported by the Army Research Office (ARO) under contract FA9550-21-F-0003. The authors would also like to acknowledge Prof. Shane Ardo for helpful discussions regarding the effect of the electric field on the (bi)carbonate anions.

References

1 IPCC, Climate Change 2014 Mitigation of Climate Change – Working Group III Contribution to the Fifth Assessment of the Intergovernmental Panel on Climate Change, 2014.
2 Y. Liu, É. Lucas, I. Sullivan, X. Li and C. Xiang, Challenges and Opportunities in Continuous Flow Processes for Electrochemically Mediated Carbon Capture, *iScience*, 2022, **25**(10), 105153.
3 N. MacDowell, N. Florin, A. Buchard, J. Hallett, A. Galindo, G. Jackson, C. S. Adjiman, C. K. Williams, N. Shah and P. Fennell, An Overview of CO2 Capture Technologies, *Energy Environ. Sci.*, 2010, **3**(11), 1645–1669.
4 D. W. Keith, G. Holmes, D. St. Angelo and K. Heidel, A Process for Capturing CO2 from the Atmosphere, *Joule*, 2018, **2**(8), 1573–1594.
5 J. Van Straelen and F. Geuzebroek, The Thermodynamic Minimum Regeneration Energy Required for Post-Combustion CO2 Capture, *Energy Procedia*, 2011, **4**, 1500–1507.
6 B. Gurkan, X. Su, A. Klemm, Y. Kim, S. Mallikarjun Sharada, A. Rodriguez-Katakura and K. J. Kron, Perspective and Challenges in Electrochemical Approaches for Reactive CO2 Separations, *iScience*, 2021, **24**(12), 103422.
7 I. A. Digdaya, I. Sullivan, M. Lin, L. Han, W. H. Cheng, H. A. Atwater and C. Xiang, A Direct Coupled Electrochemical System for Capture and Conversion of CO2 from Oceanwater, *Nat. Commun.*, 2020, **11**(1), 1–10.
8 I. Sullivan, A. Goryachev, I. A. Digdaya, X. Li, H. A. Atwater, D. A. Vermaas and C. Xiang, Coupling Electrochemical CO2 Conversion with CO2 Capture, *Nat. Catal.*, 2021, **4**(11), 952–958.
9 R. Sharifian, R. M. Wagterveld, I. A. Digdaya, C. Xiang and D. A. Vermaas, Electrochemical Carbon Dioxide Capture to Close the Carbon Cycle, *Energy Environ. Sci.*, 2021, **14**(2), 781–814.
10 H. Seo and T. A. Hatton, Electrochemical Direct Air Capture of CO2 Using Neutral Red as Reversible Redox-Active Material, *Nat. Commun.*, 2023, **14**(1), 1–11.
11 X. Li, X. Zhao, Y. Liu, T. A. Hatton and Y. Liu, Redox-Tunable Lewis Bases for Electrochemical Carbon Dioxide Capture, *Nat. Energy*, 2022, **7**(11), 1065–1075.
12 K. M. Diederichsen, Y. Liu, N. Ozbek, H. Seo and T. A. Hatton, Toward Solvent-Free Continuous-Flow Electrochemically Mediated Carbon Capture with High-Concentration Liquid Quinone Chemistry, *Joule*, 2022, **6**(1), 221–239.
13 L. E. Clarke, M. E. Leonard, T. A. Hatton and F. R. Brushett, Thermodynamic Modeling of CO2Separation Systems with

Soluble, Redox-Active Capture Species, *Ind. Eng. Chem. Res.*, 2022, **61**(29), 10531–10546.

14 Y. Liu, H. Z. Ye, K. M. Diederichsen, T. Van Voorhis and T. A. Hatton, Electrochemically Mediated Carbon Dioxide Separation with Quinone Chemistry in Salt-Concentrated Aqueous Media, *Nat. Commun.*, 2020, **11**(1), 1–11.

15 M. Rahimi, A. Khurram, T. A. Hatton and B. Gallant, Electrochemical Carbon Capture Processes for Mitigation of CO2 Emissions, *Chem. Soc. Rev.*, 2022, **51**(20), 8676–8695.

16 M. D. Eisaman, L. Alvarado, D. Larner, P. Wang, B. Garg and K. A. Littau, CO2 Separation Using Bipolar Membrane Electrodialysis, *Energy Environ. Sci.*, 2011, **4**(4), 1319–1328.

17 M. D. Eisaman, L. Alvarado, D. Larner, P. Wang and K. A. Littau, CO 2 Desorption Using High-Pressure Bipolar Membrane Electrodialysis, *Energy Environ. Sci.*, 2011, **4**(10), 4031–4037.

18 M. C. Stern, F. Simeon, H. Herzog and T. A. Hatton, Post-Combustion Carbon Dioxide Capture Using Electrochemically Mediated Amine Regeneration, *Energy Environ. Sci.*, 2013, **6**(8), 2505–2517.

19 J. H. Rheinhardt, P. Singh, P. Tarakeshwar and D. A. Buttry, Electrochemical Capture and Release of Carbon Dioxide, *ACS Energy Lett.*, 2017, **2**(2), 454–461.

20 K. M. Diederichsen, Y. Liu, N. Ozbek, H. Seo and T. A. Hatton, Toward Solvent-Free Continuous-Flow Electrochemically Mediated Carbon Capture with High-Concentration Liquid Quinone Chemistry, *Joule*, 2022, **6**(1), 221–239.

21 M. Wang, H. J. Herzog and T. A. Hatton, CO2 Capture Using Electrochemically Mediated Amine Regeneration, *Ind. Eng. Chem. Res.*, 2020, **59**(15), 7087–7096.

22 M. Rahimi, K. M. Diederichsen, N. Ozbek, M. Wang, W. Choi and T. A. Hatton, An Electrochemically Mediated Amine Regeneration Process with a Mixed Absorbent for Postcombustion CO2Capture, *Environ. Sci. Technol.*, 2020, **54**(14), 8999–9007.

23 A. P. Muroyama, A. Pătru and L. Gubler, Review—CO 2 Separation and Transport via Electrochemical Methods, *J. Electrochem. Soc.*, 2020, **167**(13), 133504.

24 B. Gurkan, X. Su, A. Klemm, Y. Kim, S. Mallikarjun Sharada, A. Rodriguez-Katakura and K. J. Kron, Perspective and Challenges in Electrochemical Approaches for Reactive CO2 Separations, *iScience*, 2021, **24**(12), 103422.

25 A. Iizuka, K. Hashimoto, H. Nagasawa, K. Kumagai, Y. Yanagisawa and A. Yamasaki, Carbon Dioxide Recovery from Carbonate Solutions Using Bipolar Membrane Electrodialysis, *Sep. Purif. Technol.*, 2012, **101**, 49–59.

26 J. C. Bui, K. R. M. Corpus, A. T. Bell and A. Z. Weber, On the Nature of Field Enhanced Water Dissociation in Bipolar Membranes, *J. Phys. Chem. C*, 2021, **125**(45), 24974–24987.

27 J. C. Bui, I. Digdaya, C. Xiang, A. T. Bell and A. Z. Weber, Understanding Multi-Ion Transport Mechanisms in Bipolar Membranes, *ACS Appl. Mater. Interfaces*, 2020, acsami.0c12686.

28 E. W. Lees, A. Liu, J. C. Bui, S. Ren, A. Z. Weber and C. P. Berlinguette, Electrolytic Methane Production from Reactive Carbon Solutions, *ACS Energy Lett.*, 2022, 1712–1718.

29 R. Sharifian, L. Boer, R. M. Wagterveld and D. A. Vermaas, Oceanic Carbon Capture through Electrochemically Induced in Situ Carbonate Mineralization Using Bipolar Membrane, *Chem. Eng. J.*, 2022, **438**, 135326.

30 H. Nagasawa, A. Yamasaki, A. Iizuka, K. Kumagai and Y. Yanagisawa, A New Recovery Process of Carbon Dioxide from Alkaline Carbonate Solution via Electrodialysis, *AIChE J.*, 2009, **55**(12), 3286–3293.

31 R. Sharifian, L. Boer, R. M. Wagterveld and D. A. Vermaas, Oceanic Carbon Capture through Electrochemically Induced in Situ Carbonate Mineralization Using Bipolar Membrane, *Chem. Eng. J.*, 2022, **438**, 135326.

32 T. Li, E. W. Lees, M. Goldman, D. A. Salvatore, D. M. Weekes and C. P. Berlinguette, Electrolytic Conversion of Bicarbonate into CO in a Flow Cell, *Joule*, 2019, **3**(6), 1487–1497.

33 A. G. Fink, E. W. Lees, Z. Zhang, S. Ren, R. S. Delima and C. P. Berlinguette, Impact of Alkali Cation Identity on the Conversion of HCO3− to CO in Bicarbonate Electrolyzers, *ChemElectroChem*, 2021, **8**(11), 2094–2100.

34 E. W. Lees, M. Goldman, A. G. Fink, D. J. Dvorak, D. A. Salvatore, Z. Zhang, N. W. X. Loo and C. P. Berlinguette, Electrodes Designed for Converting Bicarbonate into CO, *ACS Energy Lett.*, 2020, **5**(7), 2165–2173.

35 F. Sabatino, M. Gazzani, F. Gallucci and M. Van Sint Annaland, Modeling, Optimization, and Techno-Economic Analysis of Bipolar Membrane Electrodialysis for Direct Air Capture Processes, *Ind. Eng. Chem. Res.*, 2022, **61**(34), 12668–12679.

36 F. Sabatino, M. Mehta, A. Grimm, M. Gazzani, F. Gallucci, G. J. Kramer and M. Van Sint Annaland, Evaluation of a Direct Air Capture Process Combining Wet Scrubbing and Bipolar Membrane Electrodialysis, *Ind. Eng. Chem. Res.*, 2020, **59**(15), 7007–7020.

37 R. Kas, K. Yang, G. P. Yewale, A. Crow, T. Burdyny and W. A. Smith, Modeling the Local Environment within Porous Electrode during Electrochemical Reduction of Bicarbonate, *Ind. Eng. Chem. Res.*, 2022, **61**(29), 10461–10473.

38 E. W. Lees, J. C. Bui, D. Song, A. Z. Weber and C. P. Berlinguette, Continuum Model to Define the Chemistry and Mass Transfer in a Bicarbonate Electrolyzer, *ACS Energy Lett.*, 2022, **7**, 834–842.

39 M. A. Blommaert, R. Sharifian, N. U. Shah, N. T. Nesbitt, W. A. Smith and D. A. Vermaas, Orientation of a Bipolar Membrane Determines the Dominant Ion and Carbonic Species Transport in Membrane Electrode Assemblies for CO2reduction, *J. Mater. Chem. A*, 2021, **9**(18), 11179–11186.

40 M. A. Blommaert, J. A. H. Verdonk, H. C. B. Blommaert, W. A. Smith and D. A. Vermaas, Reduced Ion Crossover in Bipolar Membrane Electrolysis via Increased Current Density, Molecular Size and Valence, *ACS Appl. Energy Mater.*, 2020, **3**(6), 5804–5812.

41 V. I. Zabolotskii, S. V. Utin, K. A. Lebedev, P. A. Vasilenko and N. V. Shel'Deshov, Study of PH Correction Process of Chloride-Bicarbonate Dilute Solutions by Electrodialysis with Bipolar Membranes, *Russ. J. Electrochem.*, 2012, **48**(7), 767–772.

42 S. Z. Oener, M. J. Foster and S. W. Boettcher, Accelerating Water Dissociation in Bipolar Membranes and for Electrocatalysis, *Science*, 2020, **80**, eaaz1487.

43 É. Lucas, L. Han, I. Sullivan, H. A. Atwater and C. Xiang, Measurement of Ion Transport Properties in Ion Exchange Membranes for Photoelectrochemical Water Splitting, *Front. Energy Res.*, 2022, **10**, 1–11.
44 K. G. Schulz, U. Riebesell, B. Rost, S. Thoms and R. E. Zeebe, Determination of the Rate Constants for the Carbon Dioxide to Bicarbonate Inter-Conversion in PH-Buffered Seawater Systems, *Mar. Chem.*, 2006, **100**(1–2), 53–65.
45 N. P. Craig, *Electrochemical Behavior of Bipolar Membranes*, 2013.
46 J. Newman and K. E. Thomas-Alyea, *Electrochemical Systems*, John Wiley and Sons, Inc., Hoboken, NJ, 3rd edn, 2004.
47 L. Onsager and R. M. Fuoss, Irreversible Processes in Electrolytes. Diffusion, Conductance, and Viscous Flow in Arbitrary Mixtures of Strong Electrolytes, *J. Phys. Chem.*, 1932, **36**(11), 2689–2778.
48 L. Onsager, Deviations from Ohm' s Law in Weak, *J. Chem. Phys.*, 1934, **2**, 599–615.
49 V. Kaiser, S. T. Bramwell, P. C. W. Holdsworth and R. Moessner, Onsager's Wien Effect on a Lattice, *Nat. Mater.*, 2013, **12**, 1033–1037.
50 M. Lin, I. A. Digdaya and C. Xiang, Modeling the Electrochemical Behavior and Interfacial Junction Profiles of Bipolar Membranes at Solar Flux Relevant Operating Current Densities. Sustain, *Energy Fuels*, 2021, **5**, 2149–2158.
51 A. R. Crothers, R. M. Darling, A. Kusoglu, C. J. Radke and A. Z. Weber, Theory of Multicomponent Phenomena in Cation-Exchange Membranes: Part II. Transport Model and Validation, *J. Electrochem. Soc.*, 2020, **167**(1), 013548.
52 A. R. Crothers, R. M. Darling, D. I. Kushner, M. L. Perry and A. Z. Weber, Theory of Multicomponent Phenomena in Cation-Exchange Membranes: Part III. Transport in Vanadium Redox-Flow-Battery Separators, *J. Electrochem. Soc.*, 2020, **167**(1), 013549.
53 É. Lucas, J. C. Bui, M. Hwang, K. Wang, A. T. Bell, A. Z. Weber, S. Ardo, H. A. Atwater and C. Xiang, Asymmetric Bipolar Membrane for High Current Density Electrodialysis Operation with Exceptional Stability, *ChemRxiv*, 2023, 1–33.
54 K. N. Grew and W. K. S. Chiu, A Dusty Fluid Model for Predicting Hydroxyl Anion Conductivity in Alkaline Anion Exchange Membranes, *J. Electrochem. Soc.*, 2010, **157**(3), B327.
55 S. A. Mareev, E. Evdochenko, M. Wessling, O. A. Kozaderova, S. I. Niftaliev, N. D. Pismenskaya and V. V. Nikonenko, A Comprehensive Mathematical Model of Water Splitting in Bipolar Membranes: Impact of the Spatial Distribution of Fixed Charges and Catalyst at Bipolar Junction, *J. Membr. Sci.*, 2020, **603**, 118010.
56 J. Liu, Z. Kang, D. Li, M. Pak, S. M. Alia, C. Fujimoto, G. Bender, Y. S. Kim and A. Z. Weber, Elucidating the Role of Hydroxide Electrolyte on Anion-Exchange-Membrane Water Electrolyzer Performance, *J. Electrochem. Soc.*, 2021, **168**(5), 054522.
57 H. Q. Dinh, W. L. Toh, A. T. Chu and Y. Surendranath, Neutralization Short-Circuiting with Weak Electrolytes Erodes the Efficiency of Bipolar Membranes, *ACS Appl. Mater. Interfaces*, 2022, **15**(3), 4001–4010.
58 D. A. Vermaas, S. Wiegman and W. A. Smith, Ion Transport Mechanisms in Bipolar Membranes for (Photo)Electrochemical Water Splitting. Sustain, *Energy Fuels*, 2018, **9**, 2006–2015.
59 A. Kusoglu and A. Z. Weber, New Insights into Perfluorinated Sulfonic-Acid Ionomers, *Chem. Rev.*, 2017, **117**(3), 987–1104.
60 J. Peng, A. L. Roy, S. G. Greenbaum and T. A. Zawodzinski, Effect of CO2 Absorption on Ion and Water Mobility in an Anion Exchange Membrane, *J. Power Sources*, 2018, **380**, 64–75.
61 É. Lucas, J. C. Bui, M. Hwang, K. Wang, A. T. Bell, A. Z. Weber, S. Ardo, H. A. Atwater and C. Xiang, Asymmetric Bipolar Membrane for High Current Density Electrodialysis Operation with Exceptional Stability, *ChemRxiv*, 2023, 1–33.
62 A. Hodges, A. L. Hoang, G. Tsekouras, K. Wagner, C.-Y. Lee, G. F. Swiegers and G. G. Wallace, A High-Performance Capillary-Fed Electrolysis Cell Promises More Cost-Competitive Renewable Hydrogen, *Nat. Commun.*, 2022, **13**(1), 1304.
63 A. Nouri-Khorasani, E. Tabu Ojong, T. Smolinka and D. P. Wilkinson, Model of Oxygen Bubbles and Performance Impact in the Porous Transport Layer of PEM Water Electrolysis Cells, *Int. J. Hydrogen Energy*, 2017, **42**(48), 28665–28680.
64 E. W. Lees, B. A. W. Mowbray, F. G. Parlane and C. P. Berlinguette, Gas Diffusion Electrodes and Membranes for CO2 Reduction Electrolysers, *Nat. Rev. Mater.*, 2021, 55–64.
65 Z. D. Wei, M. B. Ji, S. G. Chen, Y. Liu, C. X. Sun, G. Z. Yin, P. K. Shen and S. H. Chan, Water Electrolysis on Carbon Electrodes Enhanced by Surfactant, *Electrochim. Acta*, 2007, **52**(9), 3323–3329.
66 K. Zeng and D. Zhang, Recent Progress in Alkaline Water Electrolysis for Hydrogen Production and Applications, *Prog. Energy Combust. Sci.*, 2010, **36**(3), 307–326.
67 Z. Zhang, E. W. Lees, F. Habibzadeh, D. A. Salvatore, S. Ren, G. L. Simpson, D. G. Wheeler, A. Liu and C. P. Berlinguette, Porous Metal Electrodes Enable Efficient Electrolysis of Carbon Capture Solutions, *Energy Environ. Sci.*, 2022, **15**(2), 705–713.
68 R. B. Bird; W. E. Stewart and E. N. Lightfoot, *Transport Phenomena*, Wiley, New York, USA, 2nd edn, 2002.
69 P. Sforza, *Drag Estimation*, 2014.
70 M. E. Q. Pilson, *Introduction to Chemistry of the Sea*, Cambridge University Press, Cambridge, UK, 2nd edn, 1998.
71 Z. B. Zhang, B. A. W. Mowbray, C. T. E. Parkyn, Y. Kim and C. P. Berlinguette, Electrolytic Cement Clinker Production Sustained through Orthogonalization of Ion Vectors, *ChemRxiv*, 2023, preprint, DOI: **10.26434/chemrxiv-2023-0zcw9**.
72 T. Rijnaarts, N. T. Shenkute, J. A. Wood, W. M. De Vos and K. Nijmeijer, Divalent Cation Removal by Donnan Dialysis for Improved Reverse Electrodialysis, *ACS Sustainable Chem. Eng.*, 2018, **6**(5), 7035–7041.
73 M. Park, J. Park, E. Lee, J. Khim and J. Cho, Application of Nanofiltration Pretreatment to Remove Divalent Ions for Economical Seawater Reverse Osmosis Desalination, *Desalin. Water Treat.*, 2016, **57**(44), 20661–20670.

74 M. R. Gerhardt, L. M. Pant, J. C. M. Bui, A. R. Crothers, V. M. Ehlinger, J. C. Fornaciari, J. Liu and A. Z. Weber, Methods—Practices and Pitfalls in Voltage Breakdown Analysis of Electrochemical Energy-Conversion Systems, *J. Electrochem. Soc.*, 2021, **168**(7), 074503.
75 P. Goyal, A. Kusoglu and A. Z. Weber, Coalescing Cation Selectivity Approaches in Ionomers, *ACS Energy Lett.*, 2023, **8**(3), 1551–1566.
76 D. Powers, A. N. Mondal, Z. Yang, R. Wycisk, E. Kreidler and P. N. Pintauro, Freestanding Bipolar Membranes with an Electrospun Junction for High Current Density Water Splitting, *ACS Appl. Mater. Interfaces*, 2022, **14**(31), 36092–36104.
77 L. Chen, S. Z. Oener, K. Fabrizio and S. W. Boettcher, Design Principles for Water Dissociation Catalysts in High-Performance Bipolar Membranes, *Nat. Commun.*, 2022, **13**, 1–10.

